DISCLAIMER

This report was prepared as an account of work sponsored by an agency of the United States Government. Neither the United States Government nor any agency thereof, nor any of their employees, makes any warranty, express or implied, or assumes any legal liability or responsibility for the accuracy, completeness, or usefulness of any information, apparatus, product, or process disclosed, or represents that its use would not infringe privately owned rights. Reference herein to any specific commercial product, process, or service by trade name, trademark, manufacturer, or otherwise does not necessarily constitute or imply its endorsement, recommendation, or favoring by the United States Government or any agency thereof. The views and opinions of authors expressed herein do not necessarily state or reflect those of the United States Government or any agency thereof. Reference herein to any social initiative (including but not limited to Diversity, Equity, and Inclusion (DEI); Community Benefits Plans (CBP); Justice 40; etc.) is made by the Author independent of any current requirement by the United States Government and does not constitute or imply endorsement, recommendation, or support by the United States Government or any agency thereof.

SAND2026-15526

SANDIA REPORT

SAND2026-xxxx
Printed December 2025

Sandia National Laboratories

Probabilistic Predictions for Fastener Failure in the Sandia Mechanics Challenge Using the Discrete-Direct Uncertainty Quantification Approach

John P. Mersch, Vicente J. Romero & Edmundo Corona

Prepared by
Sandia National Laboratories
Albuquerque, New Mexico 87185
Livermore, California 94550

Issued by Sandia National Laboratories, operated for the United States Department of Energy by National Technology & Engineering Solutions of Sandia, LLC.

Available to DOE and DOE contractors from

U.S. Department of Energy
Office of Scientific and Technical Information
P.O. Box 62
Oak Ridge, TN 37831

Telephone: (865) 576-8401
Facsimile: (865) 576-5728
E-Mail: reports@osti.gov
Online ordering: http://www.osti.gov/scitech

Available to the public from

U.S. Department of Commerce
National Technical Information Service
5301 Shawnee Road
Alexandria, VA 22312

Telephone: (800) 553-6847
Facsimile: (703) 605-6900
E-Mail: orders@ntis.gov
Online order: https://classic.ntis.gov/help/order-methods

ABSTRACT

This paper documents the blind and post-blind analysis predictions for the 2023 Sandia Mechanics Challenge (SMC), which involved predicting the behavior of a threaded fastener joint structure subjected to shock loading. Utilizing repeat sets of fastener calibration data from various experimental configurations including tension, double shear, and joint tension, we developed a library of calibrated models which were propagated through the application model using the Discrete-Direct (DD) uncertainty quantification (UQ) approach. Although the initial blind predictions did not incorporate spare-sample processing to quantify fastener failure probabilities, the analyses yielded reasonable conclusions aligned with experimental results.

In the post-blind analysis phase, we focused on enhancing the fidelity of the aluminum constitutive model and innovating the DD approach to obtain probabilistic predictions for fastener failure, particularly when quantities of interest (QoIs) approach their bounds. The improved aluminum model captures the behavior of the cantilever under shock loading more accurately, predicting both partial and complete cracks, although it tends to underpredict failure propagation. The enhanced DD approach facilitates probabilistic predictions that reflect the interdependent failure mechanisms of the fasteners and the cantilever, revealing that while certain fasteners are more likely to fail, the failure does not necessarily follow a progressive pattern.

Overall, the post-blind analyses significantly improved the predictive capabilities of the model, providing valuable insights into the SMC application and establishing a robust foundation for informed engineering decisions. The methodology demonstrates a cost-effective and extensible approach suitable for a wide range of applications, highlighting the importance of uncertainty quantification to provide context for engineering decision making.

This page intentionally left blank.

ACKNOWLEDGEMENT

A big thank you to the members of the original blind prediction team: Paul Miles, David Najera, Robert Kuether, and Joseph Bishop. Your contributions and teamwork are much appreciated!

We would like to acknowledge the use of SandiaAI Chat for edits and revisions to my documentation.

Sandia National Laboratories is a multi-mission laboratory managed and operated by National Technology and Engineering Solutions of Sandia, LLC., a wholly owned subsidiary of Honeywell International, Inc., for the U.S. Department of Energy's National Nuclear Security Administration under contract DE-NA0003525.

This page intentionally left blank.

CONTENTS

Acknowledgement **5**

Acronyms & Definitions **13**

1. Introduction **15**

2. The Sandia Mechanics Challenge and Blind Predictions **17**
2.1. SMC Background 17
2.1.1. Calibration 19
2.1.2. SMC Challenge Geometry Modeling 24
2.1.3. Blind Predictions 25
2.1.4. SMC Experimental Results 26
2.1.5. Blind Prediction Comparison and Lessons Learned 27

3. Post-Blind Modeling and Calibration **29**
3.1. Aluminum 29
3.2. Fastener Modeling 35

4. Discrete Direct and Simultaneous Discrete Direct Approaches for Model Calibration, Uncertainty Propagation, and UQ **37**
4.1. Overview 37
4.2. Simultaneous Discrete-Direct Method 41
4.3. Application of SDD Methodology to the Fasteners Calibration-UQ Problem 42

5. Drop Table Analysis Predictions **47**

6. Discussion and Conclusions **53**

References **55**

Appendices **59**

A. Blind Prediction Calibration Results **59**
A.1. Reasonable Bounds on Bolt Failure Probabilities from Sparse Realizations of Failures and/or Non-Failures within the Variability of Predicted Responses 60

This page intentionally left blank.

LIST OF FIGURES

Figure 2-1. Analysis model of the SMC structure. 17
Figure 2-2. Tension and shear analysis models for the fastener characterization tests. 20
Figure 2-3. Joint tension analysis model. 21
Figure 2-4. Fraction of failure ranges in drop table analyses as a function of test number from data packet. 25
Figure 2-5. EQPS contours for aluminum cantilever and block. 26
Figure 2-6. Summary of failure mechanisms in the SMC experiments. 27

Figure 3-1. Measured and predicted uniaxial, quasi-static engineering stress-strain curves at $T = 25°C$ and at 100°C. 30
Figure 3-2. Measured and predicted uniaxial stress strain curves initially at $T = 25°C$ and $\dot{\varepsilon} = 0.001$ (isothermal) and 630 1/s (adiabatic). 31
Figure 3-3. Notched tension test load-deflection and failure calibration results. 32
Figure 3-4. Hat specimen compression load-deflection and failure calibration results including micrographs (from [1]) the four corners of the test sections through the center of the specimen. 32
Figure 3-5. Effect of element size and type. 34

Figure 4-1. Simplified representation of the Discrete-Direct model calibration-propagation-UQ paradigm. 38
Figure 4-2. Propagation of $N = 3$ calibration parameter sets of $D = 2$ parameters each. 39
Figure 4-3. Simultaneous DD example with $N = 2$ calibration tests and DD calibrations for each of $M = 3$ submodels to be used in a system model. 41
Figure 4-4. Two possible combinations where $N = 2$ experiments and DD calibrations for each submodel are used once and only once in $N = 2$ system-level simulations to get $N = 2$ predictions (realizations) of response variability. Calibration parameter sets are designated as vectors in this figure to signify that each calibration problem may have multiple calibration parameters. 42
Figure 4-5. All four possible combinations for the $N = 2$ $M = 3$ SDD calibration and uncertainty propagation problem where each submodel test and calibration is used once and only once in system-level simulations to obtain N predictions (realizations) of response variability. 43

Figure 5-1. Bolt probability of failure as a function of velocity change 47
Figure 5-2. Progressive failure of aluminum cantilever for increasing shock pulse, with figures colored by $Damage$. 49
Figure 5-3. Back of cantilever for Test 16 analysis result, with figure colored by $Damage$. . . 50
Figure 5-4. Failure mechanisms in the SMC analyses 51

Figure A-1. Calibration results for slow double shear test data. 59
Figure A-3. Calibration results for fast tension test data 59
Figure A-2. Calibration results for slow tension test data. 60
Figure A-4. Calibration results for fast/slow joint tension test data 60
Figure A-5. Binomial distribution for $N = 5$ draws from a binomial population with $P = 0.4$. Outcome probabilities (histogram bar heights) are [0.07776, 0.2592 , 0.3456 , 0.2304 , 0.0768 , 0.01024]. 61
Figure A-6. Low and high reasonable values for the proportion of failures in an asymptotically large binomial population that yields the indicated numbers of failure realizations in the indicated number N of random draws from the population. . . 63
Figure A-7. Scalar data samples, tolerance interval, and equivalent normal distribution 64

LIST OF TABLES

Table 2-1. Test data from SMC [2] 18
Table 2-2. Aluminum material parameters. 19
Table 2-3. Insert and washer density and elastic parameters. 19
Table 2-4. Test data and analysis naming convention. 22
Table 2-5. Fastener density and elastic parameters. 22
Table 2-6. Fastener rate-dependent parameters. [3] 23
Table 2-7. Fastener parameters for Voce model – slow double shear (SDS) fasteners. 23
Table 2-8. Fastener parameters for Voce model – slow tension (ST) fasteners. 23
Table 2-9. Fastener parameters for Voce model – fast tension (FT) fasteners. 23
Table 2-10. Fastener parameters for Voce model – fast/slow joint (FSJ) fasteners. 23

Table 3-1. Material parameters for Al6061 with Hill plasticity model. 33

Table 4-1. SDD parameter set groupings for $N = 2$ runs of system model under special case of $M = 3$ nominally identical components and associated submodels in the system, with example parameter grouping corresponding to Combination 2 in Figures 4-4 and 4-5. 43
Table 4-2. SDD example combination of calibration parameter sets for $N = 5$ simulations of Cantilever Beam Drop-Table test. 44
Table 4-3. Row fractions of failure for each bolt in the structural model for Drop-Table Test 17 shock conditions from [2] and Table 4-2's row calibration parameter sets assigned to the bolts. 44
Table 4-4. Reliably conservative estimates of the probabilities of reaching the failure condition $fof = 1$ for each bolt in the structural model using samples from Test 17 analysis. 45
Table 4-5. A second set of SDD parameter sets groupings for $N = 5$ simulations of cantilever beam drop-table test. 45
Table 4-6. Row fractions of failure for each bolt in the structural model for drop-table test 17 shock conditions and Table 4-5 row calibration parameter sets assigned to the bolts. 45
Table 4-7. Reliably conservative estimates of the probabilities of reaching the failure condition $fof = 1$ for each bolt in the structural model. 46

This page intentionally left blank.

ACRONYMS & DEFINITIONS

DD Discrete-Direct

EQPS Equivalent Plastic Strain

FJ Fast Joint Tension

FT Fast Tension

MPC Multi-Point Constraints

SDD Simultaneous Discrete-Direct

TIEN Tolerance Interval Equivalent Normal

TIEN90 Tolerance Interval Equivalent Normal at 90

g Acceleration due to gravity

NGW Next Generation Workflow

QoI Quantities of Interest

SDS Slow Double Shear

SM Solid Mechanics

SJ Slow Joint Tension

ST Slow Tension

SMC Sandia Mechanics Challenge

UQ Uncertainty Quantification

This page intentionally left blank.

1. INTRODUCTION

The Sandia Mechanics Challenge (SMC) was issued at the 17th U.S. National Congress on Computational Mechanics in Albuquerque, NM in July 2023 [2]. The SMC offers participants an opportunity to predict the behavior of a complex geometry subjected to diverse loading conditions, testing the participants' predictive capabilities and providing a forum for teams to socialize their approaches within the larger engineering analysis community. For the 2023 challenge, the geometry involved a threaded fastener joint structure subjected to a shock environment. The jointed structure is attached to the carriage of a bungee-accelerated drop table, where the carriage impacts a reaction mass and transmits a shock loading to the structure of interest. Participants were invited to predict the behavior of the structure through blind predictions of various quantities of interest (QoIs), including the failure of the fasteners, joints, and jointed structure.

The first author led a Sandia team that formulated a strategy to answer the challenge questions while being mindful of time and budget constraints [4] [5]. The team focused primarily on modeling fastener failure and utilized the "Discrete-Direct" (DD) uncertainty quantification (UQ) approach [6], an approach developed at Sandia for UQ with large analysis models where model calibration data and computer cycles are limited. The DD approach has been successfully applied to similar fastener analysis problems [7], but one of the challenges for this type of fastener analysis is that the tolerance interval equivalent normal (TIEN) sparse-sampling statistical processing method [8] cannot be applied to bounded quantities of interest (QoIs) when a significant portion of the QoI output realizations reach a bound. This limitation is sometimes encountered in abnormal mechanical fastener analyses and complicates probabilistic predictions for quantities like fastener failure. Although the team did not fully utilize the capabilities of the DD approach for the initial SMC blind predictions, i.e., no sparse-sampling statistical processing was used to quantify probabilities of fastener failure, the reduced application of the DD approach resulted in competitive and insightful engineering predictions for the challenge [4] [5]. However, the team identified two key areas for improvement in the analysis before the challenge results were released: first, the aluminum model had not undergone rigorous calibration; second, the DD approach could be enhanced to better quantify fastener failure probabilities, particularly when a significant portion of the fastener QoIs reach their failure bound.

This paper documents the blind and post-blind SMC analysis. First, the blind-prediction process is documented and the initial results are summarized. Then, the post-blind investigations are detailed which target improving the fidelity of the aluminum constitutive model and innovating the DD approach to obtain probabilistic predictions for fastener failure. The aluminum constitutive model is improved by calibrating rate and temperature-dependent plasticity and failure models. Although this new aluminum model is only calibrated for predicting the initiation of failure, it is extended in this application to predict failure propagation in the absence of a better model. The DD approach is enhanced to extend to the conservative prediction of failure probabilities when QoIs have significant

samples at a bound, leveraging relevant binomial distributions. This enhancement is applied to the primary QoI of fastener fractional nearness to failure (fof) where $0 \leq fof \leq 1$.

The blind-prediction analyses provide adequate results that can be used to make sound engineering judgements, and these predictions are improved in the post-blind analyses which reasonably capture relevant QoIs in the SMC with probabilistic uncertainty information. Post-blind predictions of fastener failure, which were not calibrated to the SMC results in any way, fall within similar velocity-change regions as test data, and the fastener probabilities of failure obtained from the DD approach reflect test occurrences, including some tests passing within velocity-change regions of concern and subsets of fasteners failing (not “all or nothing"). The predictions relating to the failure of the aluminum cantilever also correlate well with test data even though the constitutive model utilized is not calibrated for failure propagation. Failure initiation of the aluminum in the analysis closely resembles test data, and although failure propagation appears to occur more slowly in the analysis, predictions are close enough to test data that credible engineering decisions could have been made in the absence of any test information. Overall, these results showcase a strong approach to fastener modeling that is conducive to component and system-level analysis.

2. THE SANDIA MECHANICS CHALLENGE AND BLIND PREDICTIONS

2.1. SMC Background

The Sandia Mechanics Challenge provides participants the opportunity to analyze the behavior of a complex structure and submit blind predictions documenting the expected behavior. The 2023 SMC, documented thoroughly in [2], [1], and [5], focuses on a geometry comprised of a 6061 aluminum block and cantilever connected by six NAS1351-3-12P fasteners. Washers and Keenserts are included with each joint. This geometry is shown in Figure 2-1, where the 6061 aluminum cantilever is grey, the 6061 aluminum block is red, the fasteners are blue, and the cadmium-plated stainless steel washers are orange. Not shown in the figure are the six stainless steel Keenserts which sit in the aluminum block. The fastener numbering convention is also noted in the figure for identification of individual fasteners in the configuration.

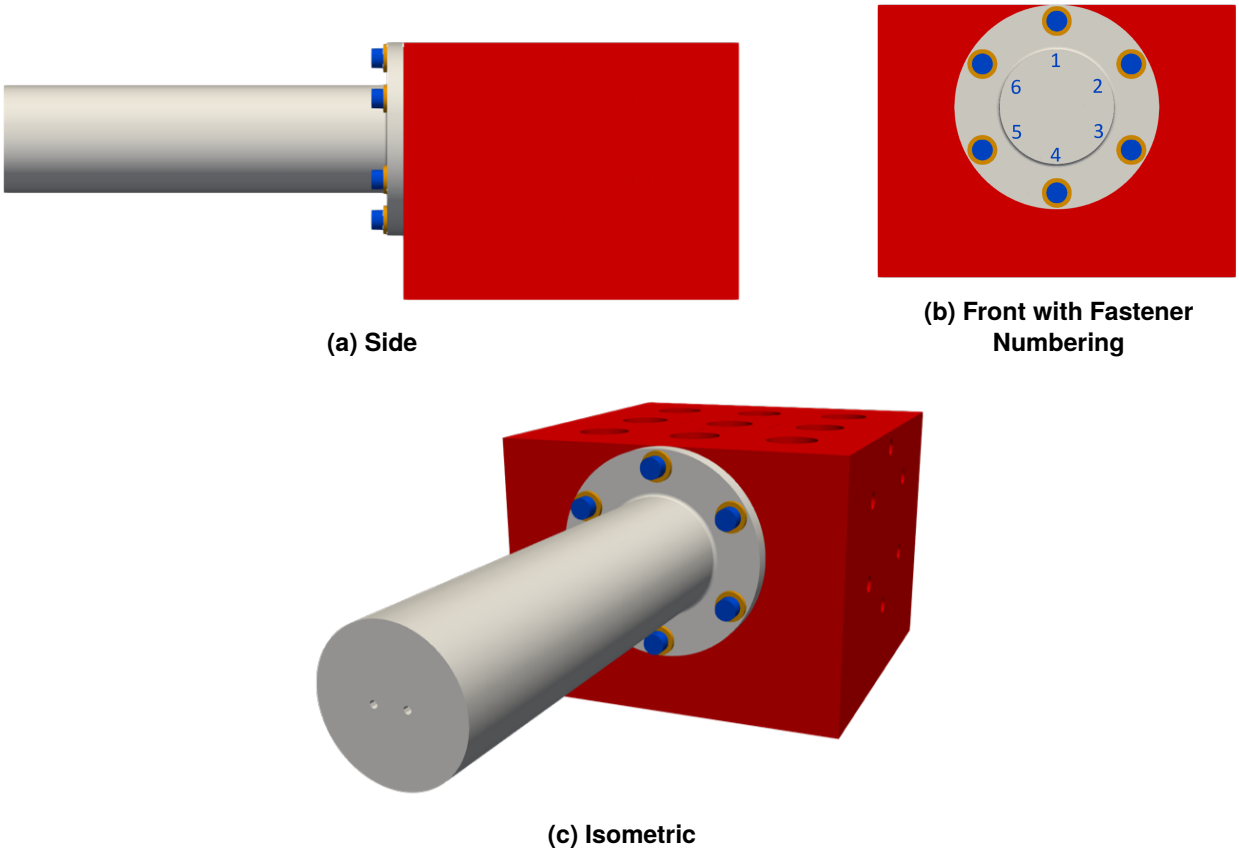

(a) Side

(b) Front with Fastener Numbering

(c) Isometric

Figure 2-1. Analysis model of the SMC structure.

The SMC structure is subjected to a shock environment via a bungee-accelerated drop table, and challenge participants are invited to predict the behavior of the structure as the shock environment increases in severity. Nineteen total shock tests were provided as part of the initial SMC data packet [2], and the test specifications are detailed in Table 2-1. Shocks range in magnitude from approximately 5150g to 11900g and changes in velocity range from 43.2 ft/s to 127.9 ft/s. A rich set of characterization data is made available to the participants to calibrate constitutive models for the fasteners and aluminum. The experimental configurations for the fasteners include fastener tension, fastener double shear, single joint tension, and single joint shear. For the aluminum, there are experimental data for tension, top hat shear-compression, and Kolsky bar tests. Some of the tests listed above are performed at various rates to facilitate rate-dependent constitutive model calibration. Additional documentation of the lead author's blind-prediction models and approaches are detailed in [4].

Table 2-1. Test data from SMC [2]

Test	Velocity Change (ft/s)	Peak Acceleration (g)	Impact Duration (ms)
1	43.2	5151	0.46
2	50.0	5995	0.45
3	54.2	6312	0.46
4	60.0	7388	0.44
5	63.7	7449	0.44
6	66.4	9209	0.33
7	70.8	8634	0.43
8	77.9	8562	0.49
9	82.6	9567	0.46
10	85.2	10030	0.45
11	89.1	10858	0.43
12	95.9	10670	0.46
13	98.8	11924	0.43
14	103.9	11692	0.45
15	105.6	11860	0.45
16	109.1	11578	0.49
17	114.9	10080	0.64
18	119.7	11114	0.65
19	127.9	8774	0.88

SMC participants are invited to answer many different questions about the structure when subjected to the shocks detailed in Table 2-1, including when the first fastener in the structure will fail, when all fasteners will fail, will any failure occur in the cantilever, and will any failure occur in the block and/or the Keenserts. For the blind predictions, the team primarily focused on the failure predictions of the fasteners, but also made statements about the integrity of the cantilever, Keenserts, and block.

2.1.1. Calibration

An anisotropic model is calibrated for the aluminum block. Material parameters for this aluminum model are provided in Table 2-2, which is calibrated using MatCal [9], an automated Sandia tool for calibration. Note that the density of the aluminum is varied in the SMC analyses for the block and the cantilever to accurately capture the mass of the components after geometric simplications are made for ease of meshing. Inserts and washers are modeled using elastic properties of 304 stainless steel [10] and those material parameters are provided in Table 2-3.

Table 2-2. Aluminum material parameters.

Property	Value
Density (lb-s^2/in^4)	0.000254
Young's Modulus (psi)	1.00E+07
Poisson's Ratio	0.33
Yield Stress (psi)	50725.69031
Hardening Modulus (psi)	13050.35321
Exponential Coefficient	17.15961961
r_{11}	0.90458
r_{22}	0.90458
r_{33}	1
r_{12}	1
r_{23}	1
r_{31}	1
$EQPS_{\text{FAIL,33}}$	0.675
$EQPS_{\text{FAIL,22}}$	0.29

Table 2-3. Insert and washer density and elastic parameters.

Material Property	Value
Density (lb-s^2/in^4)	0.000741
Young's Modulus (psi)	28,500,000
Poisson's Ratio	0.27

Three experimental configurations are used to calibrate constitutive model parameters for the fasteners: fastener tension, fastener double shear, and joint tension. The analysis models for the fastener tension and fastener double shear experiments are shown in Figure 2-2 and the analysis model for the joint tension configuration is shown in Figure 2-3. Fasteners are modeled with a "plug" approach, where cylinders represent the head and shank and there is no explicit modeling of threads. The plug's shank diameter is the nominal diameter of the fastener. Note that uniform-gradient hexahedral elements are used for the fastener in the fastener tension and fastener double shear calibrations, and selective deviatoric elements with deviatoric parameter = 0.5 are utilized for the fastener in the joint tension calibrations. The reason selective deviatoric elements were used for the joint tension calibrations is because that set of calibration data was released at a later date,

and in between SMC data releases a peer reviewer suggested changing the element formulation in the fasteners.

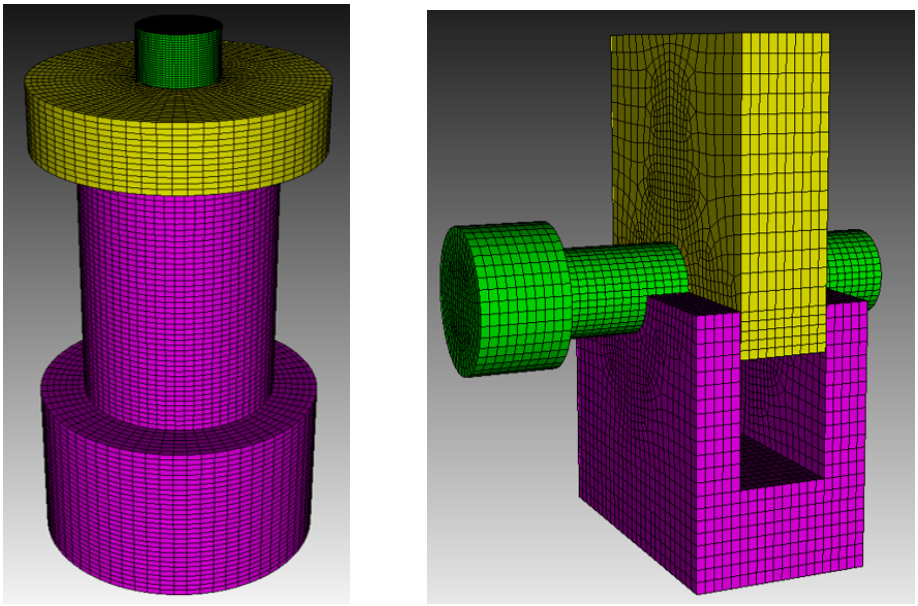

(a) Tension **(b) Double Shear**

Figure 2-2. Tension and shear analysis models for the fastener characterization tests.

The tension and shear experimental configurations utilize steel fixturing. The tension-dominated joint test is intended to represent the application joint, and thus uses similar materials, inserts, and washers. The top and bottom fixtures for the joint (grey and red in Figure 2-3) are Al6061-T6. The stainless steel washer and stainless steel Keensert (not shown in Figure 2-3) are the same as those present in the challenge geometry. Fasteners are preloaded to 60 in-lb within the structure prior to testing. The bottom part of the fixture (red in Figure 2-3) is connected to a rod and clevis to allow for slight rotations of the fixturing. This mechanism for rotation is captured with the pink rod and cyan pin shown in Figure 2-3. The cyan pin is fixed on both ends, but the pink rod is free to rotate around the pin. Displacement is applied vertically to the two flat, long rectangular surfaces of the grey body near the top of the volume (see Figure 2-3) . The fasteners are modeled with the same geometry and mesh discretization as what is used in the application model. All simulations are performed in Sierra Solid Mechanics (SM) [11].

J2-plasticity models with Voce hardening and power-law breakdown rate dependence are calibrated for the fasteners. Note that parameters for the strain-rate-dependent power law breakdown model are not calibrated here, but are inherited from previous work for similar fasteners [3]. The calibration process for the Voce hardening model is performed using Dakota [12] to drive an automated Next Generation Workflow (NGW) analysis workflow [13]. The Voce hardening model and power law breakdown model are given by equations 2.1 and 2.2, respectively:

$$\tilde{\sigma} = \sigma_y + A\left(1 - e^{-n\bar{\epsilon}^p}\right) \tag{2.1}$$

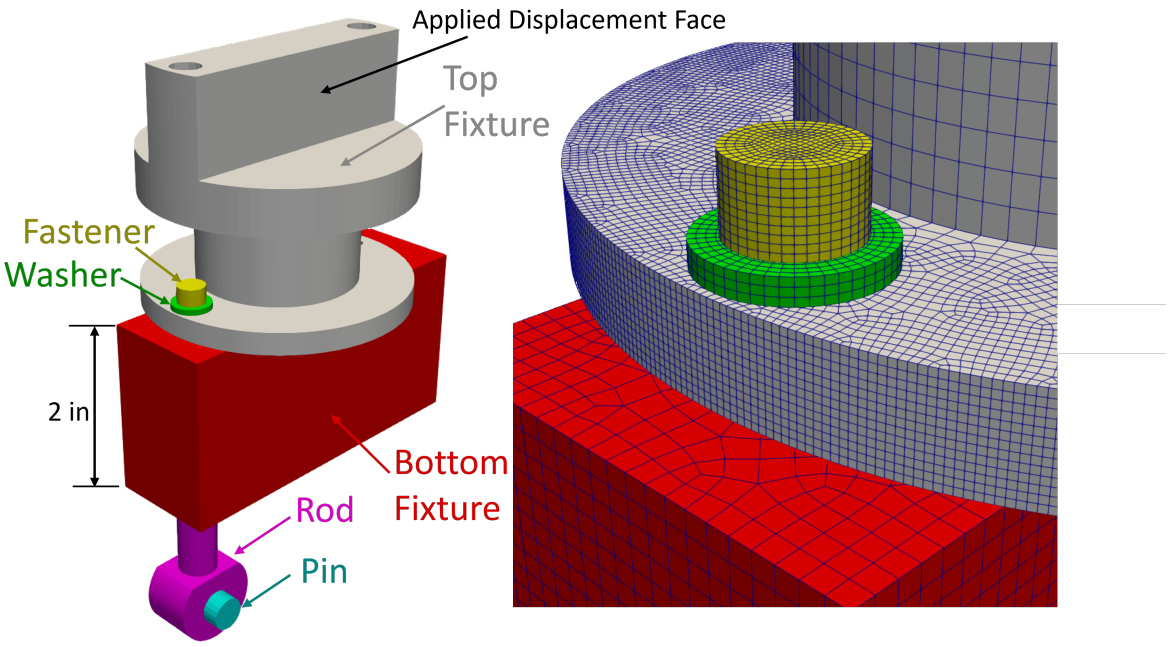

Figure 2-3. Joint tension analysis model.

$$\bar{\sigma} = \tilde{\sigma}\left(\bar{\epsilon}^p\right)\left[1 + \sinh^{-1}\left(\left(\frac{\dot{\bar{\epsilon}}^p}{g}\right)^{\frac{1}{m}}\right)\right] \tag{2.2}$$

where in Equation (2.1), $\tilde{\sigma}$ is the rate-independent flow stress, σ_y is the yield stress, A is the hardening modulus, n is the exponential coefficient, and $\bar{\epsilon}^p$ is the effective plastic strain. In Equation (2.2), $\bar{\sigma}$ is the flow stress, $\dot{\bar{\epsilon}}^p$ is the effective plastic strain rate, g model parameter related to the activation energy required to transition from climb to glide-controlled deformation, and m dictates the strength of the dependence [14].

There are 4-5 sets of test data from each of the experimental configurations used for calibration, and calibrations are performed directly to each discrete set of test data. These sets of test data are listed in Table 2-4 with their shorthand analysis names which include SDS (“slow double shear"), ST (“slow tension"), FT (“fast tension"), SJ (“slow joint" tension) and FJ (“fast joint" tension). Note that two types of the fastener tension tests (ST and FT) are used for calibration where the tests are performed at different rates, although this difference in rate is not included in the calibration process. Also, the team decided to combine the FJ and SJ datasets because there was no discernable difference in the peak loads achieved in the tests. The raw test data are manipulated to account for any compliance discrepancies between the test data and analysis response. To best calibrate the plastic response of the fastener, we scale and shift the test data such that the elastic response of the test data (after loss of preload) and analysis model are approximately equal. Preload is not included in the calibration analysis model. Note that eight-noded, uniform gradient hexahedral elements are used for all fastener models except for the joint tension calibrations, which use selective-deviatoric hexehedral elements with deviatoric parameter = 0.5.

Table 2-4. Test data and analysis naming convention.

Test Data Info	Analysis Name
double shear, 0.05 in/sec, dataset 2	SDS02
double shear, 0.05 in/sec, dataset 3	SDS03
double shear, 0.05 in/sec, dataset 4	SDS04
double shear, 0.05 in/sec, dataset 5	SDS05
tension, 0.5 mil/sec, 30 in-lb preload, dataset 1	ST01
tension, 0.5 mil/sec, 30 in-lb preload, dataset 2	ST02
tension, 0.5 mil/sec, 30 in-lb preload, dataset 3	ST03
tension, 0.5 mil/sec, 30 in-lb preload, dataset 4	ST04
tension, 0.5 mil/sec, 30 in-lb preload, dataset 5	ST05
tension, 5.0 mil/sec, 30 in-lb preload, dataset 1	FT01
tension, 5.0 mil/sec, 30 in-lb preload, dataset 3	FT03
tension, 5.0 mil/sec, 30 in-lb preload, dataset 4	FT04
tension, 5.0 mil/sec, 30 in-lb preload, dataset 5	FT05
single joint tension, 0.01 in/sec, 60 in-lb preload, dataset 1	FJ01
single joint tension, 0.01 in/sec, 60 in-lb preload, dataset 3	FJ03
single joint tension, 0.001 in/sec, 60 in-lb preload, dataset 2	SJ02
single joint tension, 0.001 in/sec, 60 in-lb preload, dataset 3	SJ03
single joint tension, 0.001 in/sec, 60 in-lb preload, dataset 4	SJ04

Calibration results are plotted in Appendix A with the corresponding test data, where the end of both the red test curve and dashed blue analysis curve indicate where failure occurs. Assumed elastic properties are listed in Table 2-5 and the rate dependent properties inherited from previous work [3] are given in Table 2-6. Note that since the nominal area of the bolt is modeled, the elastic modulus of the fastener is reduced to account for the larger model area compared to the tensile stress area of the bolt. Calibrated material parameters for the datasets listed in Table 2-4 are provided in Tables 2-7–2-10. An equivalent plastic strain (EQPS) death criterion is used to reproduce fastener failure. The critical EQPS value is unique to each fastener calibration and is obtained by inspecting the test and analysis load-displacement curves and choosing a value near experimental failure displacements. Values are chosen slightly prior to experimental failure to account for the analysis curves not falling as rapidly after ultimate stress (and thus absorbing more energy).

Table 2-5. Fastener density and elastic parameters.

Material Property	Value
Density (lb-s^2/in^4)	0.00074
Young's Modulus (psi)	20,600,000
Poisson's Ratio	0.3

Table 2-6. Fastener rate-dependent parameters. [3]

Material Property	Value
Rate Multiplier	power_law_breakdown
Rate Coefficient (psi)	1.50E+08
Rate Exponent	5.5

Table 2-7. Fastener parameters for Voce model – slow double shear (SDS) fasteners.

Analysis Name	SDS02	SDS03	SDS04	SDS05
Yield Stress (psi)	70182.09	67812.67	61765.4	74073.97
Hardening Modulus (psi)	49795.83	54249.93	58386.55	45511.61
Exponential Coefficient	53.594	47.837	66.82	40.47
EQPS Fail	0.235	0.258	0.295	0.26

Table 2-8. Fastener parameters for Voce model – slow tension (ST) fasteners.

Analysis Name	ST01	ST02	ST03	ST04	ST05
Yield Stress (psi)	114505.4	115648.2	117260.9	111229.5	117260.9
Hardening Modulus (psi)	21505.6	21224.26	20915.8	25040.6	20915.8
Exponential Coefficient	89.52	98.23	77.36	97.98	73.87
EQPS Fail	0.33	0.279	0.359	0.345	0.344

Table 2-9. Fastener parameters for Voce model – fast tension (FT) fasteners.

Analysis Name	FT01	FT03	FT04	FT05
Yield Stress (psi)	132444	130828.5	132444	130828.5
Hardening Modulus (psi)	2182.35	3724.4	2962.5	5911.39
Exponential Coefficient	143.13	137.78	121.47	141.93
EQPS Fail	0.237	0.217	0.238	0.227

Table 2-10. Fastener parameters for Voce model – fast/slow joint (FSJ) fasteners.

Analysis Name	FJ01	FJ03	SJ02	SJ03	SJ04
Yield Stress (psi)	93870.17	89421.12	102686	101646.6	84005.4
Hardening Modulus (psi)	59974.15	66551.13	44097.05	43067.12	66338
Exponential Coefficient	22.61	19.91	31.37	24.09	26.343
EQPS Fail	0.327	0.206	0.255	0.204	0.193

2.1.2. SMC Challenge Geometry Modeling

The analysis model for the SMC structure is shown in Figure 2-1. The shock loading is applied using acceleration-time histories provided for the shock loadings in the SMC. Fasteners are modeled with a plug approach derived from the calibration models. The fasteners are contiguously meshed to stainless steel inserts, which are then connected to the aluminum block holes through tied multi-point constraints (MPCs). A cadmium-plated stainless steel washer is present under each fastener. Fastener element type is dependent on the element type used for calibration — eight-noded, uniform-gradient hexahedral elements are used for the fastener tension and fastener double shear calibrations and eight-noded, selective-deviatoric hexahedral elements with deviatoric parameter = 0.5 [11] are used when leveraging the joint tension calibrations. The cantilever, washers, and inserts are meshed with eight-noded, uniform-gradient hexahedral elements. The aluminum block is meshed with 10-node composite tetrahedral elements. The analysis model contains approximately 1.88M elements.

Fastener failure is predicted by calculating the scalar QoI "fractional nearness to failure" (fof) of the i-th fastener

$$fof_i = \frac{\max(\text{EQPS}_i)}{\text{EQPS}_{\text{FAIL},i}} \tag{2.3}$$

where $\max(\text{EQPS})_i$ is the maximum value of the element variable EQPS in the entirety of the i-th fastener, and $\text{EQPS}_{\text{FAIL},i}$ is the calibrated failure criterion for the i-th fastener listed in Tables 2-7 – 2-10. Thus, $0 \leq fof \leq 1$ and we deem a fastener "failed" once one element in the fastener has reached its critical value. This value is calculated for each of the six fasteners in the SMC structure, and using the DD sampling approach explained in Section 4, a probability of failure can be calculated for each fastener at the specified test input. Note that the full methodology will be utilized in the post-blind results detailed in Section 5, but for the blind predictions only the DD sampling approach will be used to explore variability in the simulations and bound fof for each test input.

The aluminum and fastener calibrations from section 3.1 and 3.2 are used for the aluminum cantilever and fasteners, respectively. The aluminum anisotropic model calibrated in the original work [4] [5] is used for the aluminum block. Material parameters for this aluminum model are provided in Table 2-2. Inserts and washers are modeled using elastic properties of 304 stainless steel [10] and provided in Table 2-3.

Various engineering simplifications are made to the challenge geometry, including the removal of some holes to ease the meshing process. Densities of the cantilever and block are slightly adjusted to maintain accurate masses within the model as features are removed. The experimental acceleration-time history from an accelerometer attached to the drop-table carriage is applied to the bottom of the fixture block in the model. Preload is applied to the fasteners through an initial implicit simulation, and then an explicit dynamics simulation is conducted for the shock loading. All simulations are performed in Sierra SM [11].

2.1.3. Blind Predictions

Using the Discrete-Direct uncertainty quantification approach described in section 4, the sets of constitutive model parameters outlined in Tables 2-7 – 2-10. are propagated through the application model. This sampling process is repeated for each group of fastener calibrations, and sampling only takes place within a family of calibrations, e.g., only sampling from the SDS calibrations for the first study, only sampling from the ST fasteners for the second study, etc. The sampling studies for each test input from the SMC include 20-25 simulations for each family of fasteners, depending on the number of calibrations in the set (four or five). The results of fof are collected, and the ranges of fof are plotted for each family of calibration data as a function of SMC test as shown in Figure 2-4. Results are shown for bolts 1, 2, 3, and 4, noting that this model is geometrically symmetric (not necessarily materially symmetric due to the DD sampling) — results for bolt 2 and 3 are representative of results for bolts 6 and 5, respectively.

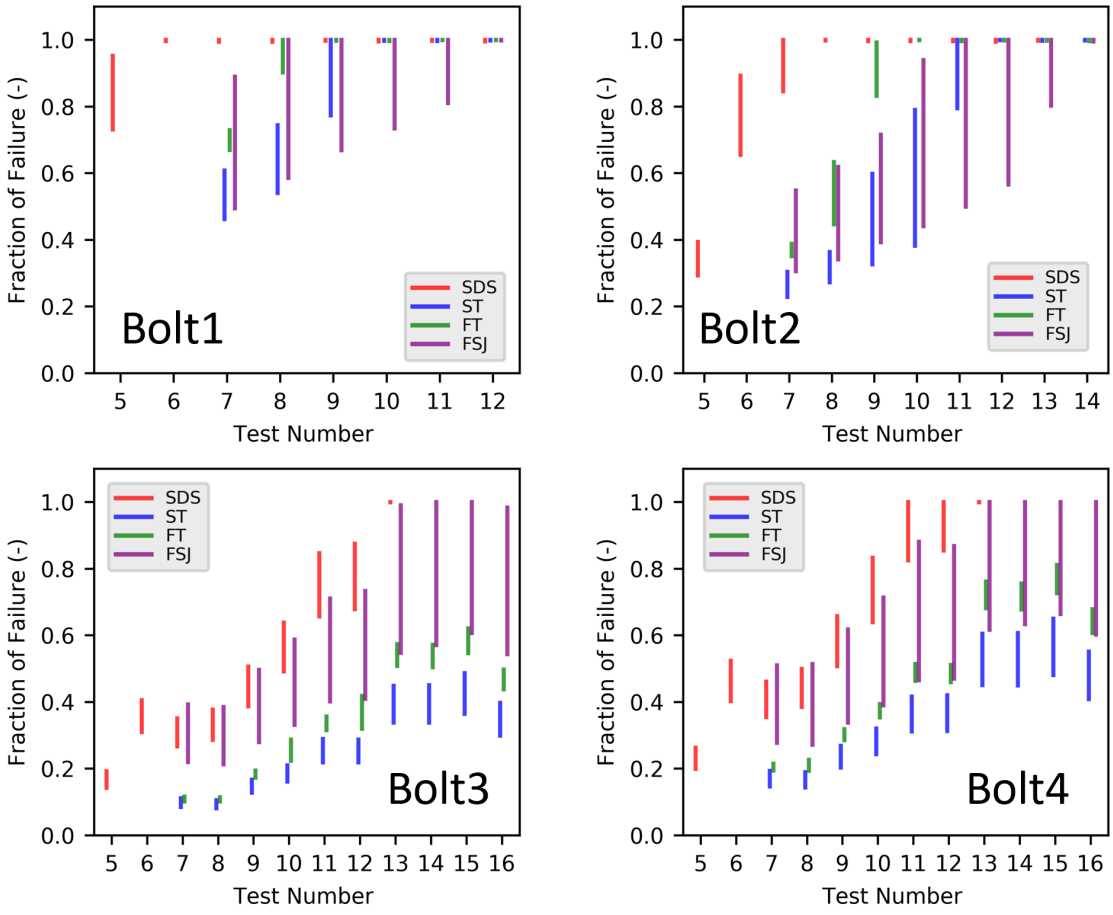

Figure 2-4. Fraction of failure ranges in drop table analyses as a function of test number from data packet.

The fof ranges shown in Figure 2-4 can then be coupled with engineering judgement to draw conclusions about what will happen to the fasteners for each test input. The plots suggest Bolt 1 will likely fail first, and the SDS sampling suggests this could be as early as Test 6 (all simulations have fof near 1.0). However, the other sets of calibration data suggest that failure will take place at

higher shock levels, maybe around Test 8 to Test 12, depending how much conservatism is desired in the answer. Since Bolt 1 is above the bending axis and likely loaded more in bending and tension, Our team chose to lean more on the tensile calibration results and conservatively predicted the first fastener failure to occur around Test 8 or 9.

When determining which tests are likely to fail all fasteners, we must consider each plot in Figure 2-4. The loading applied to the fasteners changes as we move lower on the array (Bolt 1 at the top, Bolt 4 on the bottom as illustrated in Figure 2-1), and thus we could choose to weigh different calibrations results differently for each bolt. The Bolt 2 results in Figure 2-4 suggest failure somewhere between Test 11 to Test 14. The plots for Bolt 3 and 4 suggest that failure could occur around Test 12 to Test 16, but also that there is a reasonable probability that failure may not occur. Our team chose to predict all fastener failure at Test 15, noting that some sets of calibrated parameters suggest that all fasteners may not fail.

Simulation results focusing on the behavior of the cantilever and block are presented in Figure 2-5 for Test 15 shock input (105.6 ft/s velocity change) using the ST fastener calibrations. These results indicate that significant plasticity will occur in the cantilever, with EQPS reaching as high as 0.24 at the top of the cantilever fillet beneath bolt 1. Despite this substantial amount of plasticity, our model does not predict failure based on the aluminum properties listed in Table 2-2. Furthermore, there is no observed plasticity in the aluminum block surrounding the inserts, suggesting that pullout of the insert is unlikely.

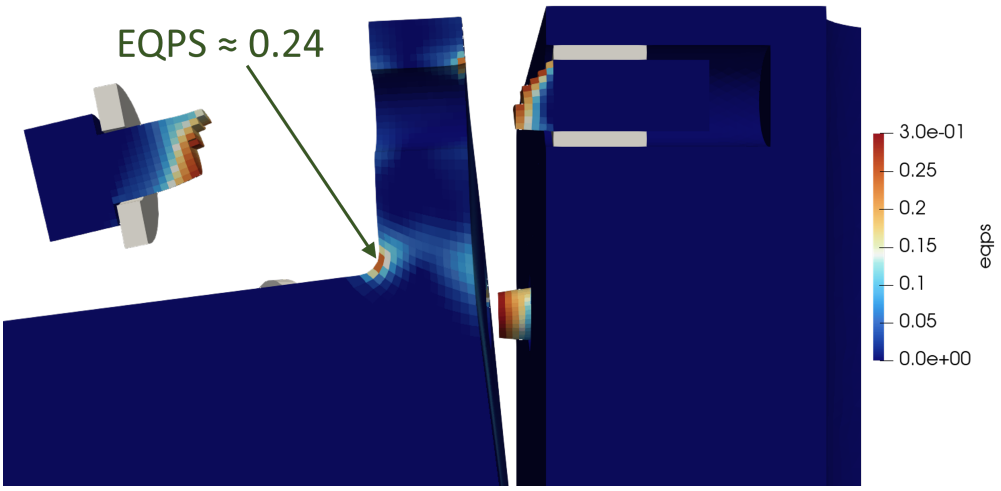

Figure 2-5. EQPS contours for aluminum cantilever and block.

2.1.4. SMC Experimental Results

The SMC experiments revealed that failures occurred in both the aluminum cantilever and the fasteners. The failure mechanisms are summarized in Figure 2-6, where aluminum failure mechanisms are categorized as “small crack", “large crack", or “through crack", and fastener failures are categorized as “partial fastener failure" (one or more fastener failures but fewer than six) and “all fastener failure". Small cracks in the aluminum cantilever begin at very small velocity-change

shocks, and through cracks begin at velocity changes of approximately 80 ft/s (around Test 9 in Table 2-1). Once the velocity change of the shock reaches approximately 100-105 ft/s (Test 14), complete failure occurs in either the fasteners or the aluminum, but not both simultaneously. In the three tests where all six fasteners failed, no aluminum failure was observed. Conversely, in the three tests with partial fastener failure, the aluminum cantilever experienced complete failure. Note that there are also tests in this velocity-change regime where fastener failure does not occur and the aluminum experiences a through crack. Thus, the results suggest that failure is stochastic in the 100-120 ft/s range and complete failure can occur in either the fasteners or the aluminum.

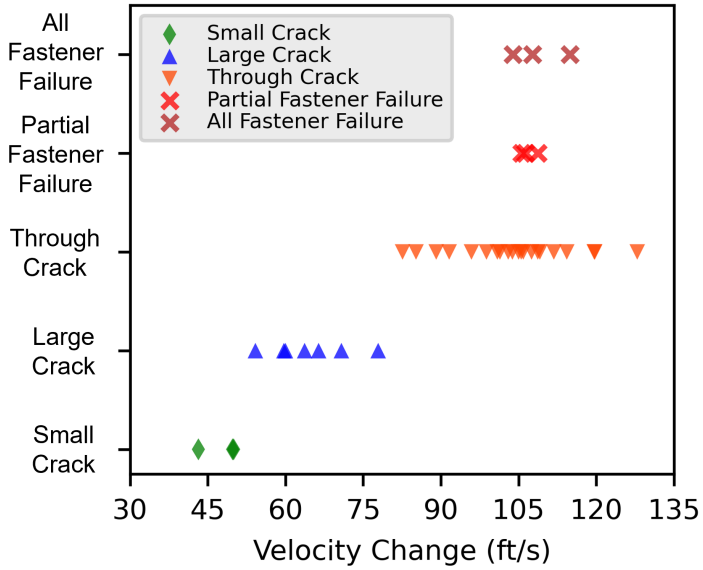

Figure 2-6. Summary of failure mechanisms in the SMC experiments.

2.1.5. Blind Prediction Comparison and Lessons Learned

Overall, the blind predictions provided acceptable results that would likely inform sound engineering decision making, especially given the scope to which the analyses were designed. Primarily, the blind-prediction team was looking to assess fastener failure, and the results suggested first fastener failure may occur around tests 9-10 (~80-85 ft/s) and all fastener failure may occur in the range of tests 13-16 (~100-110 ft/s). This is agreeable with the test data, as fastener failure occurred in the approximately 110-115 ft/s range. The main inconsistency in the fastener failure predictions is that the analyses suggest that fastener failure will occur progressively – bolt 1 should fail first at lower velocity changes, and as the shock increases in magnitude, failure will progress downward with bolts 2 and 6 failing next, and finally bolts 3, 4, and 5. However, the test series suggests that failure of the fasteners is more "all or nothing", and that fastener failure will not occur until a threshold velocity change of approximately 100 ft/s is achieved.

The other noticeable difference between the analysis and tests results is that not only does cracking occur in the cantilever, but it occurs in virtually every test and is a major failure mechanism of the

structure. While capturing this possible failure mechanism wasn't a priority of the blind-prediction team, this mechanism's role in fastener failure may have been overlooked. It was postulated by the blind-prediction team that capturing the aluminum behavior and failure better may improve the fastener failure predictions and make fastener failure less progressive.

Another observation at the conclusion of this study was that enhancing our results to be more probabilistic would enrich and contextualize the predictions. While the ranges of the fof provided in Figure 2-4 are helpful, reporting a probability of failure would offer greater value. Although the Discrete-Direct approach provides mechanisms for these calculations, challenges arise with bounded QoIs when a significant portion of the QoI reaches a bound.

Therefore, the two goals of the post-blind predictions are:

1. **Calibrate a more sophisticated constitutive model for aluminum that includes a damage model.**
2. **Enhance the DD approach to accommodate probabilistic predictions when a significant portion of the QoI is at a bound.**

These improvements are summarized in Sections 3 and 4, where Section 3 details the new aluminum constitutive model and Section 4 explains the DD approach and improvements made for quantitative uncertainty predictions when QoIs reach bounds. The post-blind results leveraging these enhancements are summarized in Section 5.

3. POST-BLIND MODELING AND CALIBRATION

This section provides an overview of the models utilized in the post-blind study. The calibration process for the new aluminum constitutive model is highlighted, which accounts for both hardening and damage. The purpose of calibrating this model is to more accurately represent the behavior of the aluminum cantilever component within the SMC challenge geometry. This section also provides a summary of which fastener models will be utilized for the post-blind investigation.

3.1. Aluminum

The calibration of the elastic-plastic material and ductile failure models for the aluminum in the cantilevered cylinder was conducted in a similar manner as outlined in [15] and [16]. The calibration process used the specimen geometries and material test results presented in [2] and [1] in a sequential approach.

The material was represented as an elastic-plastic solid with a Hill yield surface that hardens isotropically. Given the dynamic nature of loading in the challenge problem that could lead to high strain rates and self-heating of the material, the model included the effects of strain rate and temperature. Thermally, an adiabatic condition is included in the model.

The form used in the Hill plasticity model for the hardening function is that of Johnson-Cook given by

$$\bar{\sigma} = \left[\sigma_y + A(\bar{\varepsilon}^p)^n\right]\left[1 + C\ln\left(\frac{\dot{\bar{\varepsilon}}^p}{\dot{\varepsilon}_o}\right)\right]\left[1 - T^{*m}\right], \tag{3.1}$$

where $\bar{\sigma}$ is the equivalent stress and $\bar{\varepsilon}^p$ is the equivalent plastic strain.

The first term represents the hardening curve at a reference strain rate $\dot{\varepsilon}_o$ and reference temperature T_{ref}. It has a power-law form with three parameters to be calibrated: σ_y, A and n. The second term models the dependence on the equivalent plastic strain rate $\dot{\bar{\varepsilon}}^p$, where C is a calibrated parameter. The third term represents the effect of the homologous temperature T^* given by

$$T^* = \frac{T - T_{\text{ref}}}{T_{\text{melt}} - T_{\text{ref}}}, \tag{3.2}$$

with m being a parameter to be calibrated.

Figure 3-1 shows the engineering stress-strain curves from testing at the reference rate ($\dot{\varepsilon}_o = 0.001$ 1/s) and temperature ($T_{\text{ref}} = 25°\text{C}$) and at the reference rate but high temperature (100°C) in black lines. The predictions of the calibrated model are in red dashed line. Figure 3-2 similarly shows the curve at the reference rate and temperature along with one obtained at a higher strain rate ($\dot{\varepsilon} = 630$

1/s). The agreement is reasonable in all cases. The high rate simulation was conducted assuming an adiabatic condition where the temperature rise is given by

$$\Delta T = \beta^{TQ} \frac{W^p}{\rho \hat{C}}, \tag{3.3}$$

where ρ is the initial density and $\hat{C}$ is the specific heat of the material. The values of the parameters are presented in Table 3-1.

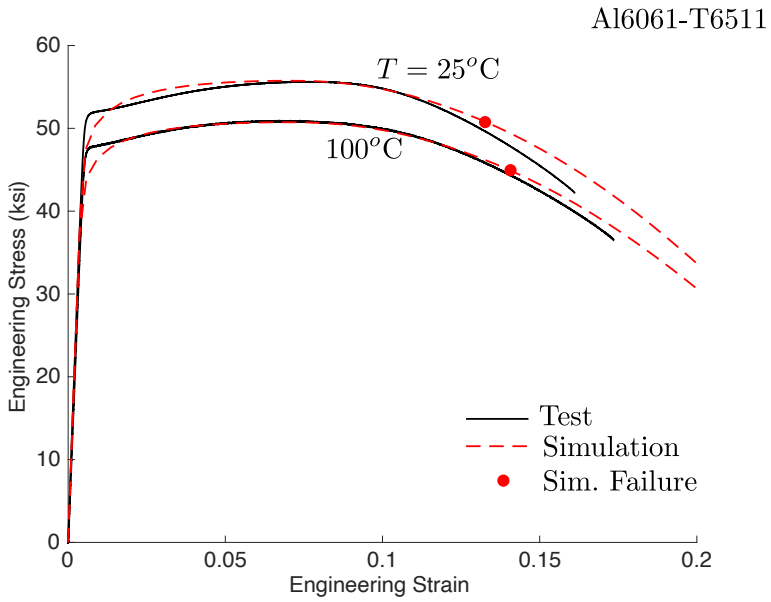

Figure 3-1. Measured and predicted uniaxial, quasi-static engineering stress-strain curves at $T = 25°$C and at $100°$C.

The model for the initiation of ductile failure is that of Wilkins [17] augmented with Johnson-Cook temperature and rate terms. It is given by

$$Damage = \frac{1}{D_{cr}} \int_0^{\bar{\varepsilon}^p} w_1 w_2 w_3 w_4 \, d\hat{\varepsilon}^p, \tag{3.4}$$

where D_{cr} is a scaling factor so failure initiates when $Damage = 1$. Next, w_1 is a function of the mean hydrostatic stress σ_m

$$w_1 = \left(\frac{1}{1 - \frac{\sigma_m}{B}} \right)^{\alpha}, \tag{3.5}$$

and has calibration parameters B and α. Next, w_2 is indirectly a function of the Lode angle given by the ratios of the principal deviatoric stresses $s_1 \geq s_2 \geq s_3$

$$w_2 = (2 - A)^{\beta} \text{ where } A = \max\left(\frac{s_2}{s_3}, \frac{s_2}{s_1} \right), \tag{3.6}$$

and the parameter β needs to be calibrated.

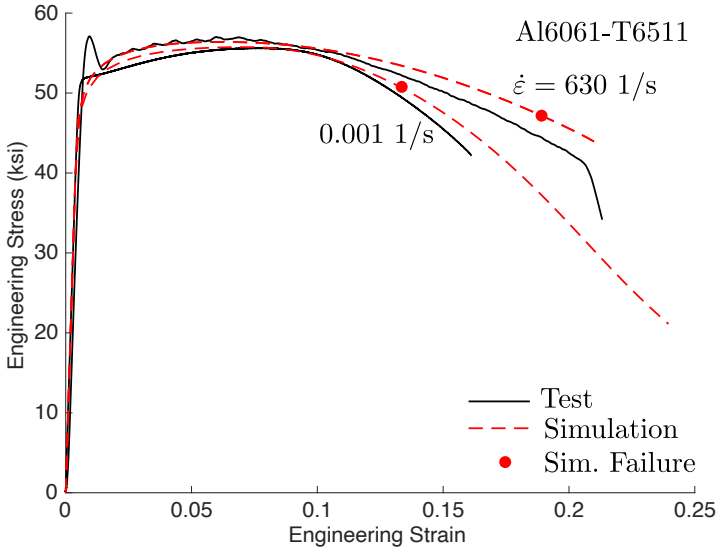

Figure 3-2. Measured and predicted uniaxial stress strain curves initially at $T = 25°$C and $\dot{\varepsilon} = 0.001$ (isothermal) and 630 1/s (adiabatic).

One of the Johnson-Cook terms models the strain rate dependence

$$w_3 = \frac{1}{1 + D_4 \ln \frac{\dot{\bar{\varepsilon}}^p}{\varepsilon_o}}, \tag{3.7}$$

and the other models the temperature dependence

$$w_4 = \frac{1}{1 + D_5 \frac{T - T_{\text{ref}}}{T_{\text{melt}} - T_{\text{ref}}}}. \tag{3.8}$$

The calibration parameters are D_4 and D_5, and T_{ref}, T_{melt} are the reference and melting temperature of the material. The fitting method for the calibration of the Wilkins parameters is outlined in [18]. It attempts to best match the displacements at failure of the the notch and hat tests in a least-squares sense. The predictions of the notch tension tests are shown in Figure 3-3 where the displacements were measured with an extensometer of initial gage length $L_g = 1$ in. Failure in the tests occurred at the end of the black lines and failure in the models is shown by the red circles. Failure initiation in the hat compression tests was determined from micrographs of the corners of the specimen at the center section, included in Fig. 3-4, in interrupted tests. The fracture propagation was stable with respect to the prescribed displacement as can be seen in the figure. Although the load-deflection prediction is not as good as those in the notched tension tests, the circle denoting failure agrees fairly well with test data, displacement-wise. Cracks in the specimen's center section become visible in the range of 0.03 to 0.04 in. of displacement. See [15] and [16] for more detailed examples of the failure model calibration.

The parameters D_4 and D_5 were calibrated from the uniaxial tension tests at temperature and rate shown in Figures 3-1 and 3-2. The circles in the plots identify the predicted failure points, which are in general a little below the displacements at failure in the tests. The values of all the parameters of the failure model are listed in Table 3-1.

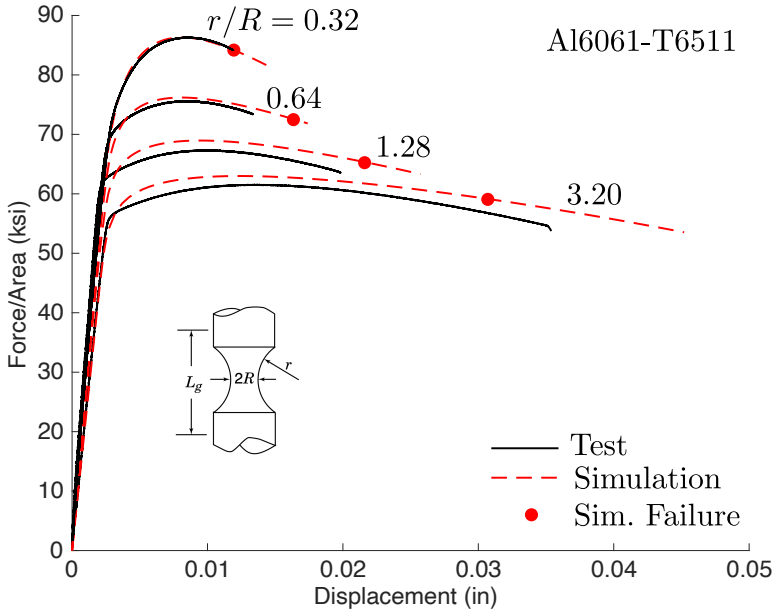

Figure 3-3. Notched tension test load-deflection and failure calibration results.

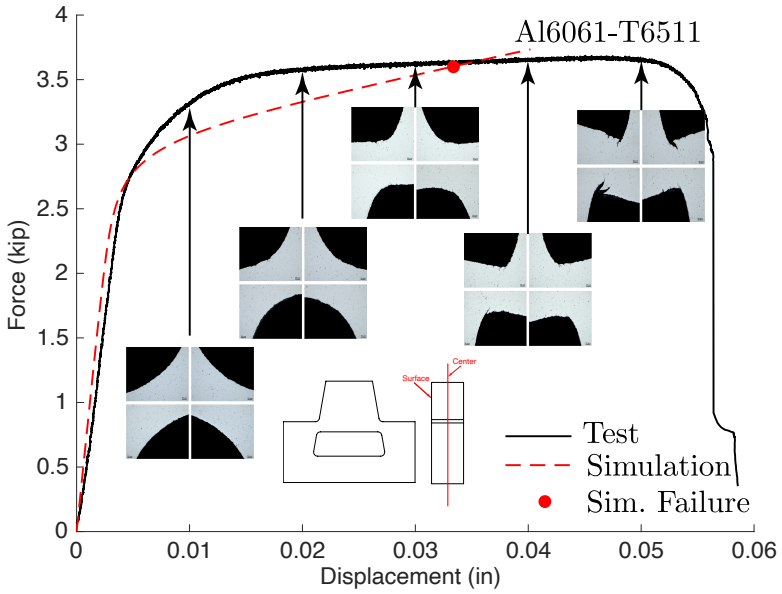

Figure 3-4. Hat specimen compression load-deflection and failure calibration results including micrographs (from [1]) the four corners of the test sections through the center of the specimen.

Table 3-1. Material parameters for Al6061 with Hill plasticity model.

Property	**Value**
Density (ρ, lb-s^2/in^4)	$1.015 \times 2.5 \times 10^{-4}$
Young's Modulus (E, psi)	10.4×10^6
Poisson's Ratio (ν)	0.33
Yield Stress (σ_y, psi)	32.5×10^3
r_{11}	0.90
r_{22}	0.90
r_{33}	1.0
r_{12}	0.90
r_{23}	0.80
r_{31}	0.80
Hardening Model	flow_stress
Isotropic Hardening Model	power_law
Hardening Constant (A, psi)	40.0×10^3
Hardening Exponent (n)	0.14
Rate Multiplier	johnson_cook
Rate Constant (C)	0.00100
Reference Rate (ε_o, 1/s)	0.001
Temperature Multiplier	johnson_cook
Melting Temperature (T_{melt}, K)	855
Reference Temperature (T_{ref}, K)	298
Temperature Exponent (m)	1.2
Thermal Softening Model	adiabatic
Specific Heat ($\hat{C}$, lb-in/(lb-s^2/in K)	(1.39×10^6)
β^{TQ}	0.9
Failure Model	modular_failure
Critical Failure Parameter	0.55
Pressure Multiplier	wilkins
Wilkins Alpha (α)	4.5
Wilkins Pressure (B, psi)	300.0×10^3
Lode Angle Multiplier	wilkins
Wilkins Beta (β)	0.6
Rate Fail Multiplier	johnson_cook
Johnson Cook D_4	0.024
Temperature Fail Multiplier	johnson_cook
Johnson Cook D_5	0.59
Element Death Criterion	Damage = 0.6

Ductile failure calculations are usually element-size dependent. Therefore, calibrations conducted with relatively fine models, as done here, must be adjusted if larger element sizes are used in applications. How to make adjustments without experimental validation exercises on the actual geometry of interest, however, has not been established systematically. The evidence that can be used is based on element size sensitivity studies on the specimen geometries used in the calibration. Figure 3-5 shows results on specimens that bracket the fillet radius of 0.05 in. at the cylinder/flange junction in the challenge geometry. These geometries include the tensile-dominated notch tension specimens with notch radii of 0.032 and 0.064 in. and the shear dominated hat specimen with fillet radius of 0.05 in. Results are presented for the element formulation used in the calibration, selective deviatoric (green lines), and also for mean quadrature elements (red lines). For element sizes in the range of 0.015 to 0.020 in., a gap can be seen between the notch and hat test results. Without a firm method to estimate the dependence of failure in the challenge geometry on element size from the results of the calibration geometries, we can only provide a loose estimate. The suggested range for the value of damage at which failure should be declared is indicated by the green rectangle, covering a range of critical damage between 0.5 and 0.8 for both element formulations. In the SMC application model, element edge lengths in the cantilever radius are approximately 0.020 in., and a death criterion of $Damage = 0.6$ is used to model failure.

Finally, it must be stated that the calibration of the failure model is applicable only to failure *initiation*. Further investigation is required to assess the failure *propagation*. In problems that are sufficiently over-driven, using the initiation criterion may be sufficient to establish complete failure, but in other problems accounting for failure propagation will be necessary if such phenomena are important.

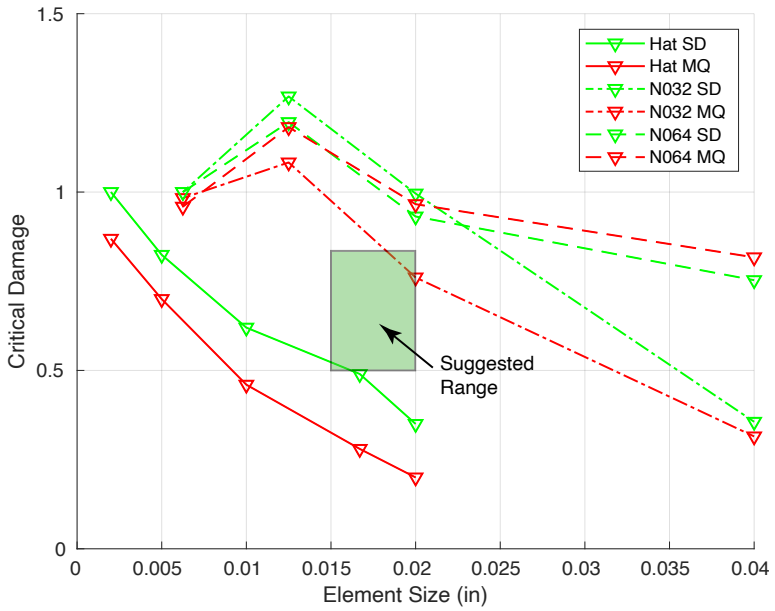

Figure 3-5. Effect of element size and type.

3.2. Fastener Modeling

Although analysis models were created for three of the calibration configurations for initial blind predictions, which included the tension, double shear, and tension-dominated single joint tests, only the tension-dominated single joint test calibrations are utilized for the post-blind analysis. These calibrated parameters led to the best predictions in the blind analysis, and the lead author believes joint-like test configurations tend to lead to the most predictive calibrated parameters. Note that the fastener material parameters derived from the tension-dominated single joint tests utilized the original aluminum material constitutive model from Table 2-2 even though we will be leveraging a new aluminum model for the post-blind analysis. The most rigorous approach would be to re-calibrate the fastener models and include the latest aluminum model and properties, but the changes are likely small, and thus we leave this for future work.

This page intentionally left blank.

4. DISCRETE DIRECT AND SIMULTANEOUS DISCRETE DIRECT APPROACHES FOR MODEL CALIBRATION, UNCERTAINTY PROPAGATION, AND UQ

This section provides an overview of the DD and Simultaneous DD (SDD) approaches that are used to quantify uncertainty of our analysis predictions for the SMC drop table tests. The use of conservative, binomial-based failure probability estimations are demonstrated here with a more thorough explanation of the procedure provided in Appendix A.1.

4.1. Overview

The DD model calibration, uncertainty propagation, and uncertainty quantification approach was developed to calibrate otherwise deterministic models to reflect unit-to-unit variability of systems being modeled that have underlying random/stochastic/aleatory variability in material properties, geometries, etc. The underlying variability causes nominally identical units to have varying behaviors and response outputs in replicate tests that provide the calibration data (after normalizing for any variations of input boundary and initial conditions from test to test). A model calibration process is used to map the experimental variability in important measured output responses into variability of one or more parameters of the model. It is common that time and resource limitations allow only a few units from a large population to be experimentally tested to supply calibration data. With only a few replicate tests to sample the stochastic variability of behaviors in the population, it is often desired to appropriately calibrate and use a model to predict response variability for the whole population of units (under various use conditions). Under these conditions, the DD calibration-propagation-UQ approach is arguably [6] the most efficient and effective of any calibration-UQ approach the authors are aware of—as summarized in the rest of this section.

Figure 4-1 presents a simplified representation of the DD calibration-UQ paradigm applied to an illustrative 1-D (one calibration variable) problem. The four deterministic experimental results in the figure come from different but nominally identical test units in four replicate tests. For now, let each test be performed at exactly the same input boundary conditions. A separate calibration is performed for each test/data set. This yields the four calibration parameter values indicated in the figure. These four values are then propagated to predictions in other modeling applications. For instance, the parameter values could be for a material model to be used under different geometry and/or initial and/or boundary conditions. The four prediction results in the figure are processed with specialized sparse-sample 1D UQ techniques (discussed later in this section) to obtain reliably conservative and efficient estimates of response variability and related statistical quantities.

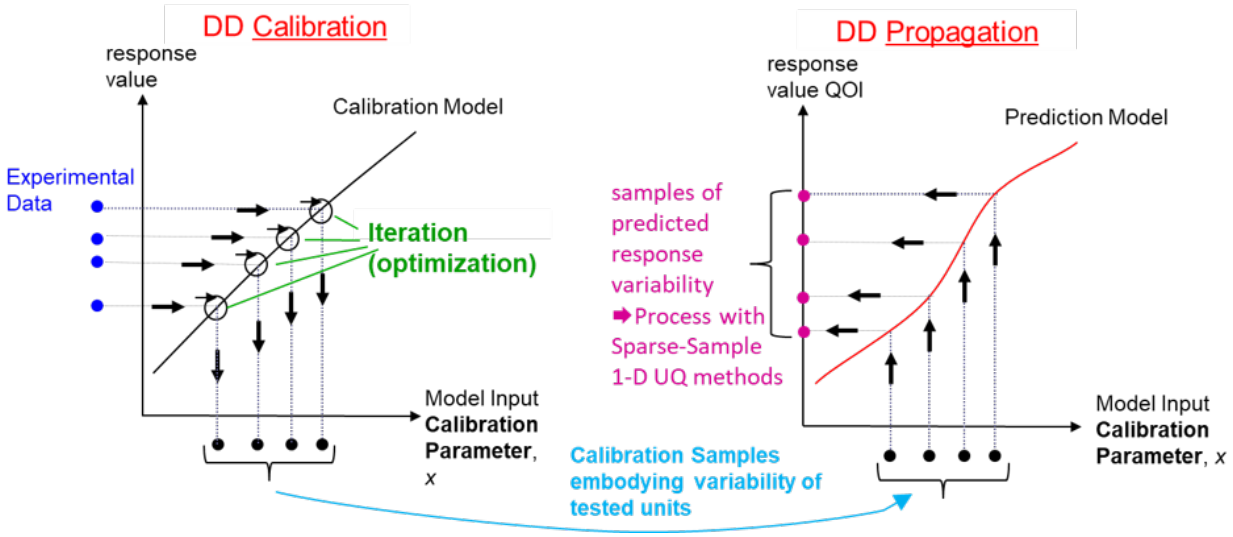

- For each replicate experiment, optimize/calibrate model parameter values for best prediction match to experimental results; N experiments $\Rightarrow$ N calibration parameter sets (here $N = 4$)
- Proceed to prediction with the N calibration parameter sets.
- Economical: N runs of prediction model to propagate N parameter sets.
- Preserves direct correspondence to the experimental data underlying the calibrations.
- Use appropriate sparse-sample 1-D UQ techniques to process N prediction results into reliably conservative distributions, or bounds on useful statistics of response variability.
- Simple to update with new experiments/data and calibrations if/when more data becomes available (without Bayes' rule & machinery).

Figure 4-1. Simplified representation of the Discrete-Direct model calibration-propagation-UQ paradigm.

DD calibration straightforwardly accommodates multiple realizations of scalar experimental data (as indicated on the ordinate at left in Figure 4-1) or functional experimental data such as load-deflection or stress-strain curves. Problems with multiple calibration parameters are also straightforwardly accommodated. For example, Figure 4-2 illustrates a propagation circumstance with $N = 3$ calibration parameter sets, each of calibration parameter dimension $D = 2$ that would arise from three calibrations where each calibration involves optimizing $D = 2$ model parameters (P1, P2). The N calibrations ostensibly[1] embody the aleatory stochastic variability in the N test specimens. Propagation of the N parameter sets yields N predictions of related response variability

[1]This assumes stable behavior in the calibrations, where sufficient identifiability exists to arrive at effectively unique values of the calibration parameters, in addition to other necessary properties of the calibration problem and procedure as discussed in [19]. We find no evidence of instability in the material model calibrations performed in the present work. Other conditions are that any experiment-to-experiment differences in boundary and initial conditions, measurement errors, etc. are appropriately accounted for in the N calibrations. In the present work, each experiment's actual measured conditions were used in the related calibrations—as they should be, and measurement errors are considered negligible relative to measured response magnitudes.

of the system as reflected in any output response QoIs. The N samples of a given QoI's response variability are processed into reliably conservative distributions, or bounds on useful statistics of response variability, using appropriate sparse-sample 1-D UQ techniques discussed later in this section.

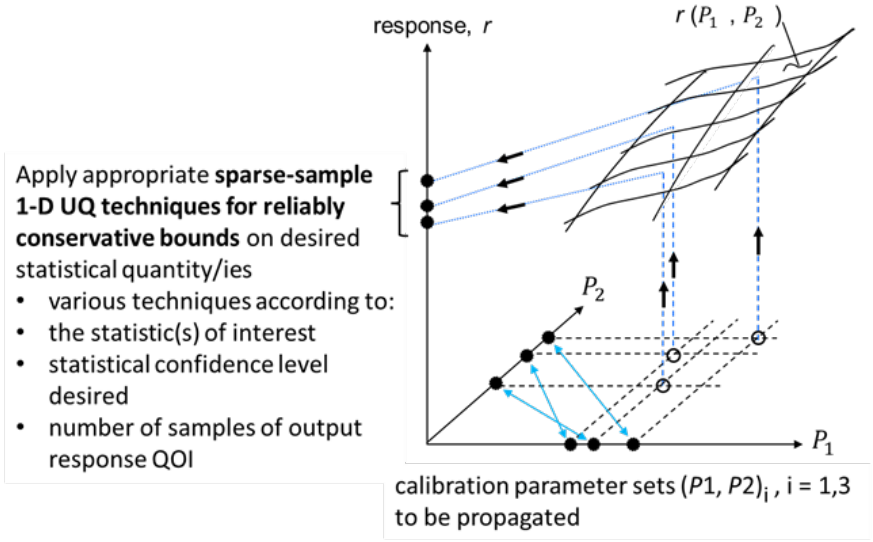

Figure 4-2. Propagation of $N = 3$ calibration parameter sets of $D = 2$ parameters each.

In contrast, consider alternative calibration-propagation-UQ approaches that would attempt to infer a joint probability density (JPD) of the calibration parameter values. Substantial difficulty, error, and complexity would accompany an attempt to infer the various hyperparameters for posed aleatory distribution forms and correlations of the $D = 2$ calibration parameters from just three tests that sample the aleatory variability of the tested units. Further complexity and expense would accompany propagation of the JPD to predictions that utilize the calibrated model. The difficulty, complexity, and expense would increase substantially as the number D of calibration parameters increases — while for DD the number N of tests, calibrations, and propagations remains three or some other affordably low number. Thus, the DD approach effectively reduces complexity and expense of nonlinear multi-dimensional uncertainty inference and propagation problems to a relatively simple and economical discrete propagation problem with 1-D sparse-sample UQ post-processing for each output quantity and statistic of interest.

Sparse-sample 1-D UQ approaches and methods to couple with DD calibration and propagation have been extensively studied and characterized for performance in conservative and efficient (not overly conservative) estimation of bounds on various statistics like distribution percentiles and tail probabilities (see [20] [21] [8] [22] [23] [24]). The estimates are intended to bound the true statistical quantities that would result from DD propagation of an asymptotically large population of calibration parameter sets from a corresponding large number of tests of the stochastically varying phenomena. The estimated bounds are obtained with well-established statistical methods based on sparse sampling of Normal populations. The extensive numerical studies just cited have established the sparse-sample UQ methods to be robust and efficient bounds estimators for the mentioned statistical quantities and diverse varieties of highly non-Normal distributions. Conversely, consider

an output response QoI probability density (PD) obtained from a propagated JPD comprising the calibration parameter marginal PDs and their correlations. The calibration parameter JPDs would have substantial error as already explained. The multiple uncharacterized errors would make it very difficult to judge whether an estimated statistic from a QoI response PD is appropriately conservative, overly conservative, or unconservative.

Another source of uncharacterized error often comes from the propagation procedure itself. A Monte Carlo (MC) sampling procedure would require orders of magnitude more runs of the analysis model than the $N = 3$ runs needed for DD propagation in the above example. A more computationally efficient alternative to pure MC propagation is to build a response-surface surrogate model and sample it in the MC propagation procedure. Depending on the nonlinearity of QoI response over the variability ranges of the calibration parameter PDs, it would require more than DD's $N = 3$ simulations with the analysis model to obtain suitably accurate response-surface MC for even just the $D = 2$ calibration parameters in our example.

Another significant advantage of a DD approach exists. Concerning the calibration parameter space, it is sometimes questionable whether it is legitimate to predict with other than actually determined parameter sets from calibration. Sometimes, analysts do not trust model prediction results obtained with synthetic calibration parameter sets. The DD approach avoids these issues and questions by propagating actual calibration parameter solution sets. On the other hand, calibration-UQ approaches built on a paradigm of propagating an inferred JPD of calibration parameter variability must interpolate and extrapolate about the actual calibration parameter solution sets that inform the inference process.

Thus, when sparse replicate tests and calibration data are involved, the DD approach is substantially simpler, typically less costly, and generally more accurate in terms of reasonably controllable and knowable statistical confidence of conservativism of calculated statistics of response quantities. DD calibration-UQ methodology has been applied at Sandia to problems involving sparse realizations of functional experimental data and 1 to 11 calibration parameters in applications in solid mechanics ([25], [26], [27], [28]); structural dynamics ([29], [19]); and radiation-damaged electronics. References [26], [27], [28], [19], [30] have been used as test problems with synthetically generated data for known truth statistics to confirm the sparse-data DD calibration-UQ methodology over thousands of random trials.

Beyond the deterministic model function and experimental data points indicated on the ordinate at left in Figure 4-1, many potential sources of error and uncertainty in the calibration model and experimental data can arise. These are itemized below. They result in uncertainty in the calibration parameter set determinable from a given experiment.

- Random and/or systematic uncertainties on measured experimental inputs and outputs
- Model discretization and solver related numerical solution uncertainties
- Uncertainties associated with approximation errors in any statistical and probability models used in the processing of the experimental data

All these uncertainties can be straightforwardly accommodated in the DD methodology as explained in [6] and demonstrated in [30]. The DD calibration and uncertainty propagation methodology

also straightforwardly reduces to handle the case of one test with no replicates but experimental uncertainties present [19].

4.2. Simultaneous Discrete-Direct Method

Next we explain the Simultaneous Discrete-Direct (SDD) method for efficient propagation and UQ when multiple material, phenomena, and/or component models of a system model are each calibrated to sparse replicate test data. Figure 4-3 shows an SDD example where two calibration tests and DD calibrations are conducted for each of three submodels to be used in a system model.

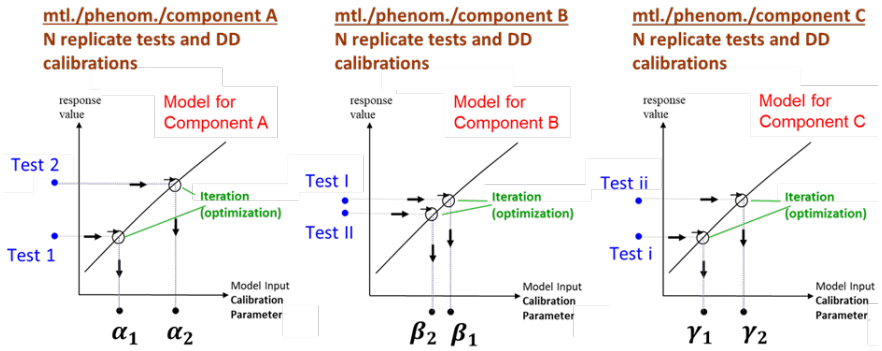

Figure 4-3. Simultaneous DD example with $N = 2$ calibration tests and DD calibrations for each of $M = 3$ submodels to be used in a system model.

Figure 4-4 shows two possible combinations of DD calibrations of submodels used in system-level predictions where each of the tests and calibration results are used once and only once. (As explained in [26], the once-and-only-once usage has an analogue to Monte Carlo propagation of probabilistic uncertainty. An advantage is empirically established vs. non-once-and-only-once usage schemes also tested and characterized in [26].) Each combination produces a number N of system-level simulations and predictions (realizations) of QoI response variability corresponding to the N tests and calibrations per submodel. Each set of N realizations of a system QoI is processed into decision-relevant statistical measures of response with 1-D sparse-sample UQ techniques discussed previously. The estimated statistic(s) from the shown combinations 1 and 2 would be different but equally legitimate; there is no reason to favor results from either combination over the other. Recent research in [26] has found that an average of such equally legitimate results is typically more accurate than individual results

For the $N = 2$ $M = 3$ SDD example, four equally legitimate combinations exist where each of N submodel tests and calibrations is used once and only once in the system-level simulations. Figure 4-5 shows the four combinations. It would take eight system model runs if one wanted to average results of all four combinations. However, it is reasonable to propagate as little as $K = 2$ or 3 such point set combinations, for a total cost of Kx$N = 4$ or 6 model runs in the present case. Appropriate 1-D UQ processing of each corresponding set of $N = 2$ QoI results yields a probabilistically reliably conservative bound on desired QoI statistics. The K estimated bounds are averaged to yield an estimate with significantly higher reliability of being conservative but not overly conservative for an economical number of additional system model runs. The goal here is to manage the risk of

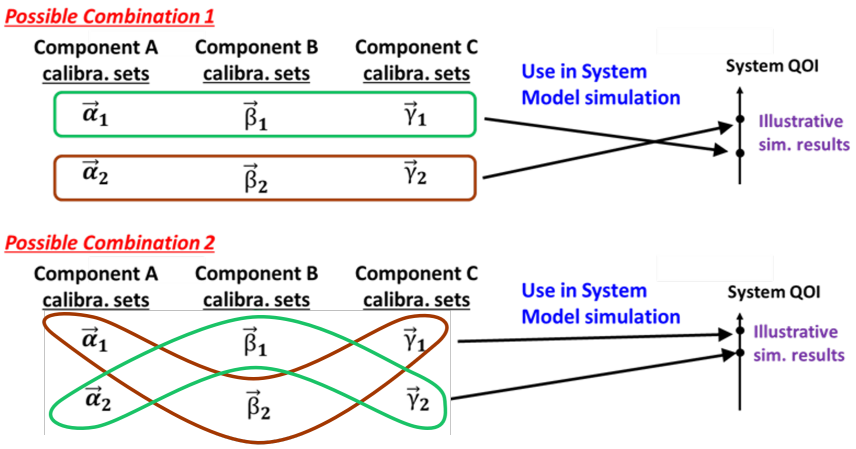

Figure 4-4. Two possible combinations where $N = 2$ experiments and DD calibrations for each submodel are used once and only once in $N = 2$ system-level simulations to get $N = 2$ predictions (realizations) of response variability. Calibration parameter sets are designated as vectors in this figure to signify that each calibration problem may have multiple calibration parameters.

non-representative extreme outcomes by chance. This can be suitably accomplished with K as little as 2. Larger K is not needed because we do not need a converged mean. Thus, the number of system model runs with SDD scales as KxN where N is the number of experiments and calibrations per each submodel of the system model. The number of calibration experiments per submodel is often just a few, as is K, so the number of system model runs is typically $<$ 10 to 20, so a system-level surrogate model is usually not necessary. The SDD approach is currently configured for experimental designs where the same number N of replicate experiments and DD calibrations are performed for each submodel. Relaxation of this constraint is currently being worked out. See [28] for an explanation of one approach.

An alternative to the SDD paradigm would be to separately calibrate the M submodels to arrive at M PDs or JPDs of calibration parameter values. These would be propagated in system-level simulations to estimate variability in response QoIs. This would be more complicated and typically more computationally expensive than the SDD approach, both in the calibrations and in system-level UQ propagation. Another disadvantage is that any over-conservatism or under-conservatism of stochastic variability approximated in the M PDs or joint PDs of calibration parameter values is unlikely to offset completely when all the PDs are propagated to system level. Compounding of over-conservatism or under-conservatism can yield highly over-conservative or under-conservative stochastic variability in response QoIs (see studies in [21], [31]).

4.3. Application of SDD Methodology to the Fasteners Calibration-UQ Problem

SDD is applied to the fasteners calibration-UQ problem per an analogue of a special case of Figures 4-3-4-5. We start by considering a special case of Figure 4-3. Consider $M = 3$ nominally identical bolts and associated behavioral submodels in a structural system model—akin to the $M = 6$ bolts in our Fasteners calibration-UQ problem. Under circumstances of $M = 3$ similar submodels, the

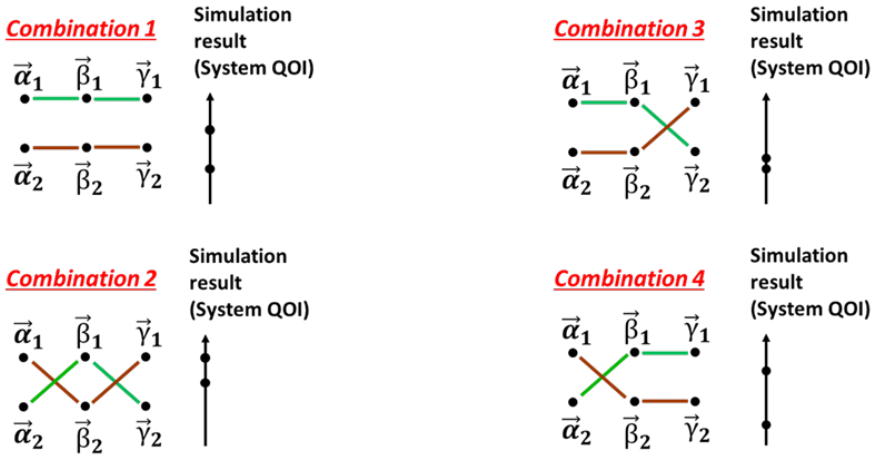

Figure 4-5. All four possible combinations for the $N = 2$ $M = 3$ SDD calibration and uncertainty propagation problem where each submodel test and calibration is used once and only once in system-level simulations to obtain N predictions (realizations) of response variability.

calibration parameter sets $\vec{\beta}_1, \vec{\beta}_2$ and $\vec{\gamma}_1, \vec{\gamma}_2$ in the figures have the same values as $\vec{\alpha}_1, \vec{\alpha}_2$. Then we can label parameter sets $\vec{\beta}_1, \vec{\beta}_2$ and $\vec{\gamma}_1, \vec{\gamma}_2$ in the figures as $\vec{\alpha}_1, \vec{\alpha}_2$. Table 4-1 presents an example.

Table 4-1. SDD parameter set groupings for $N = 2$ runs of system model under special case of $M = 3$ nominally identical components and associated submodels in the system, with example parameter grouping corresponding to Combination 2 in Figures 4-4 and 4-5.

Run	Component 1	Component 2	Component 3
Run 1 Parameter Set	$\vec{\alpha}_1$	$\vec{\alpha}_2$	$\vec{\alpha}_1$
Run 2 Parameter Set	$\vec{\alpha}_2$	$\vec{\alpha}_1$	$\vec{\alpha}_2$

In analogy, our fasteners calibration-UQ problem has $M = 6$ bolts in the system structural model. If we use the FSJ fastener calibrations from Table 2-10 as an example, each bolt in the analysis will use the same behavioral model calibrated to the $N = 5$ single-bolt fastener tests. The resulting $N = 5$ calibration parameter sets labeled FJ01,. . . ,SJ04 in Table 2-10 can be alternatively designated $\vec{\alpha}_1, \ldots, \vec{\alpha}_5$ to connect with our analogy. Table 4-2 presents an example of parameter set groupings for $N = 5$ runs of the system model where each bolt's response is informed by all $N = 5$ calibration parameter sets; each individual bolt is assigned each parameter set once and only once per DD calibration-propagation principles. The parameter sets are assigned in randomized order within each bolt column, with uncorrelated orderings between the columns.

Table 4-2. SDD example combination of calibration parameter sets for $N = 5$ simulations of Cantilever Beam Drop-Table test.

Parameter Set	Bolt 1	Bolt 2	Bolt 3	Bolt 4	Bolt 5	Bolt 6
Run 1	FJ03, $\vec{\alpha}_2$	SJ03, $\vec{\alpha}_4$	SJ02, $\vec{\alpha}_3$	SJ03, $\vec{\alpha}_4$	SJ03, $\vec{\alpha}_4$	SJ02, $\vec{\alpha}_3$
Run 2	FJ01, $\vec{\alpha}_1$	FJ03, $\vec{\alpha}_2$	SJ03, $\vec{\alpha}_4$	FJ03, $\vec{\alpha}_2$	FJ01, $\vec{\alpha}_1$	SJ03, $\vec{\alpha}_4$
Run 3	SJ02, $\vec{\alpha}_3$	SJ04, $\vec{\alpha}_5$	FJ01, $\vec{\alpha}_1$	SJ02, $\vec{\alpha}_3$	FJ03, $\vec{\alpha}_2$	FJ01, $\vec{\alpha}_1$
Run 4	SJ03, $\vec{\alpha}_4$	FJ01, $\vec{\alpha}_1$	SJ04, $\vec{\alpha}_5$	SJ04, $\vec{\alpha}_5$	SJ04, $\vec{\alpha}_5$	FJ03, $\vec{\alpha}_2$
Run 5	SJ04, $\vec{\alpha}_5$	SJ02, $\vec{\alpha}_3$	FJ03, $\vec{\alpha}_2$	FJ01, $\vec{\alpha}_1$	SJ02, $\vec{\alpha}_3$	SJ04, $\vec{\alpha}_5$

Each row in the table initiates a run of the structural model using Drop-Table Test 17 shock conditions from [2]. Each simulation yields a fof for each bolt in the model. Each bolt has $N = 5$ fof realizations shown in Table 4-3. Each bolt's fof realization depends not only on the bolt's assigned calibration parameter set (including critical EQPS value) in a given model run, but also on the global structural behavior arising from the assigned parameter sets to the other bolts per a given row of the table. The variability of fof values in Table 4-3 reflects a diversity of potential outcomes from the said random assignments of the calibration parameter sets to the bolts, in turn reflecting the test-to-test variability of the material specimens and any replicate test setup and measurement variabilities.

Table 4-3. Row fractions of failure for each bolt in the structural model for Drop-Table Test 17 shock conditions from [2] and Table 4-2's row calibration parameter sets assigned to the bolts.

	Bolt 1	Bolt 2	Bolt 3	Bolt 4	Bolt 5	Bolt 6
Run 1 Results	0.904527	0.846053	0.468061	0.707635	0.607242	0.657992
Run 2 Results	0.602032	0.775559	0.663111	0.701667	0.381975	0.879886
Run 3 Results	0.830664	0.817732	0.378650	0.564916	0.596368	0.486266
Run 4 Results	1.004880	0.515186	0.672737	0.780674	0.684075	0.821295
Run 5 Results	1.000320	0.684202	0.606004	0.438659	0.504063	0.822230

We see in Table 4-3 that Bolt 1 has two fof realizations of 1.0, indicating failure in 40% of the simulated cases. We also note that the fof response quantity has an upper limit of 1. Bounded response quantities with substantial saturation at a bound (such as 40% of occurrences here) are not optimally addressable by the sparse-sample 1-D UQ methods studied in [20] [21] [8] [22] [23] [24]. Instead, we use a binomial-based conservative failure probability estimation approach explained in Appendix A.1 where the sparse fof realizations are separated into binary categories of 'failure' and 'no failure'.

For Bolts 2–6, the fof realizations in Table 4-3 do not approach the limit of 1. Representative analysis in Appendix A.1 discounts the possibility of any meaningful failure saturation at the $fof = 1$ bound (in an asymptotically large population of response predictions for these bolts). In these cases, TIEN90 distributions (see Appendix A.1) based on the $N = 5$ fof realizations for each bolt (2 to 6) are preferred for reliably conservative estimates of the probabilities of reaching

the failure condition $fof = 1$. Table 4-4 presents conservatively estimated failure probabilities for Bolts 1–6 using the sparse-sample UQ methods summarized in Appendix A.1.

Table 4-4. Reliably conservative estimates of the probabilities of reaching the failure condition $fof = 1$ for each bolt in the structural model using samples from Test 17 analysis.

Bolt	Failure Probability
Bolt 1	Binomial reasonable min and max estimates = (0.12, 0.74)
Bolt 2	TIEN90 estimate = 0.170
Bolt 3	TIEN90 estimate = 0.055
Bolt 4	TIEN90 estimate = 0.108
Bolt 5	TIEN90 estimate = 0.036
Bolt 6	TIEN90 estimate = 0.220

Materially similar results and conclusions apply for a $K = 2$nd set of equally legitimate parameter set groupings tried for model propagations and evaluation of the bolt failure probabilities, see Tables 4-5, 4-6, 4-7.

Table 4-5. A second set of SDD parameter sets groupings for $N = 5$ simulations of cantilever beam drop-table test.

Example Combination 4	Bolt 1	Bolt 2	Bolt 3	Bolt 4	Bolt 5	Bolt 6
Sample Set 1	SJ02, $\vec{\alpha}_3$	FJ03, $\vec{\alpha}_2$	SJ03, $\vec{\alpha}_4$	FJ01, $\vec{\alpha}_1$	SJ04, $\vec{\alpha}_5$	SJ02, $\vec{\alpha}_3$
Sample Set 2	SJ04, $\vec{\alpha}_5$	SJ04, $\vec{\alpha}_5$	FJ03, $\vec{\alpha}_2$	SJ04, $\vec{\alpha}_5$	FJ01, $\vec{\alpha}_1$	SJ04, $\vec{\alpha}_5$
Sample Set 3	SJ03, $\vec{\alpha}_4$	FJ01, $\vec{\alpha}_1$	FJ01, $\vec{\alpha}_1$	FJ03, $\vec{\alpha}_2$	SJ03, $\vec{\alpha}_4$	SJ03, $\vec{\alpha}_4$
Sample Set 4	FJ01, $\vec{\alpha}_1$	SJ02, $\vec{\alpha}_3$	SJ04, $\vec{\alpha}_5$	SJ02, $\vec{\alpha}_3$	SJ02, $\vec{\alpha}_3$	FJ03, $\vec{\alpha}_2$
Sample Set 5	FJ03, $\vec{\alpha}_2$	SJ03, $\vec{\alpha}_4$	SJ02, $\vec{\alpha}_3$	SJ03, $\vec{\alpha}_4$	FJ03, $\vec{\alpha}_2$	FJ01, $\vec{\alpha}_1$

Table 4-6. Row fractions of failure for each bolt in the structural model for drop-table test 17 shock conditions and Table 4-5 row calibration parameter sets assigned to the bolts.

Example 2 Results	Bolt 1	Bolt 2	Bolt 3	Bolt 4	Bolt 5	Bolt 6
Sample Set 1	0.824765	0.758246	0.635725	0.426170	0.614001	0.669619
Sample Set 2	1.006920	0.888296	0.668552	0.794718	0.414651	0.879282
Sample Set 3	1.004440	0.493881	0.380880	0.688890	0.633988	0.847984
Sample Set 4	0.582199	0.668031	0.613456	0.552396	0.477898	0.746562
Sample Set 5	0.929188	0.860471	0.480030	0.739929	0.616997	0.495119

Table 4-7. Reliably conservative estimates of the probabilities of reaching the failure condition $fof = 1$ for each bolt in the structural model.

Bolt	Failure Probability
Bolt 1	Binomial reasonable min and max estims. = (0.12, 0.74)
Bolt 2	TIEN90 estim. = 0.218
Bolt 3	TIEN90 estim. = 0.043
Bolt 4	TIEN90 estim. = 0.131
Bolt 5	TIEN90 estim. = 0.017
Bolt 6	TIEN90 estim. = 0.205

5. DROP TABLE ANALYSIS PREDICTIONS

Analysis predictions of the probability of failure for each individual bolt are plotted as a function of velocity change in Figure 5-1, where we perform a DD propagation for each of the shock environments from tests 7-19 in the SMC (Table 2-1) using the methodology described in Section 4. The lines on the plot represent the probability of failure of a bolt in the challenge geometry calculated at the SMC-specific velocity changes, creating piecewise-linear curves. The circles represent test results from the SMC, where green circles indicate tests where no fasteners failed, and red circles indicate tests where some number of fasteners failed. The number of fasteners failed in the tests are recorded on the y axis on the right of the plot. Note that both the pulse duration and pulse magnitude change for the pulses prescribed in the SMC, so the severity of the pulses can be hard to determine and do not necessarily increase with an increase in the velocity change.

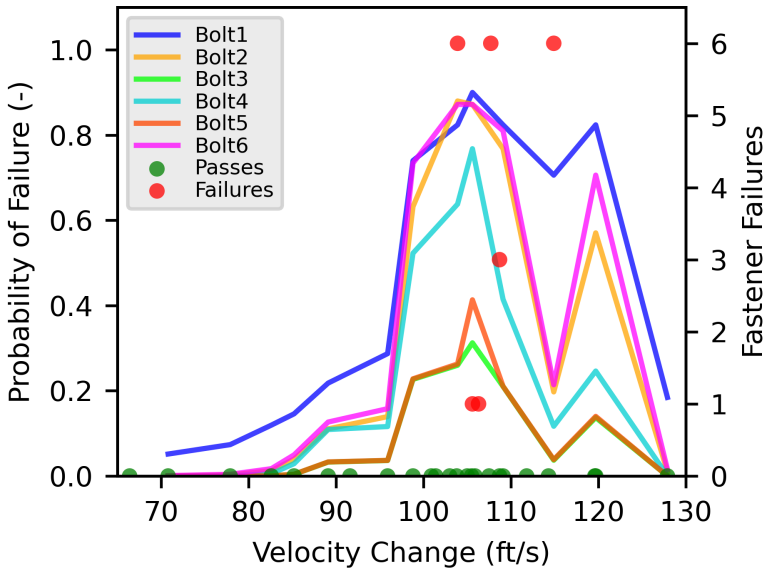

Figure 5-1. Bolt probability of failure as a function of velocity change

The probabilities of failure obtained from the analyses align reasonably well with the test data. Probabilities of failure for four of the bolts (1,2,4, and 6) eclipse 50% failure probability at a velocity change of 98.8 ft/s, and the first experimental failure occurs at 103.9 ft/s. Probabilities of failure never reach 100%, and some bolts are more likely to fail than others, which is consistent with the test data — there are tests conducted with very similar test specifications, and sometimes no fasteners fail and other times one or more fasteners fail. Notably, the dip in the analysis predictions around 115 ft/s corresponds to the red circle where all six fasteners failed. However, there is clear variability in the test results that is accurately captured in the entirety of the analysis predictions.

While the probabilities of failure may not be rigorously consistent with the test data, qualitative trends are reasonably consistent with the testing series. The analysis predictions would likely lead to decision making that is consistent with what occurred in the testing. Using Figure 5-1 as a guide, an analyst could reasonably predict 95-120 ft/s as the velocity-change region in which failure of a subset of fasteners might likely occur, and the experimental data failure range is 104-115 ft/s.

Another question posed in the SMC is to detail the behavior of the aluminum cantilever, and whether or not failure occurs. While this was not originally prioritized during the initial blind investigation due to time and funding constraints, the post-blind investigation team utilized an improved aluminum model (detailed in Section 3) to more accurately capture behavior of the cantilever, which experimentally begins to crack at low velocity changes near the top of the fillet between the cylinder and flange. This crack eventually propagates to the back side of the flange. However, this failure initiation and propagation was not predicted in the initial blind investigation.

Using the new aluminum model, the predicted damage evolution in the cantilever as the shock load increases can be observed in Figure 5-2, which depicts images of the cantilever for SMC tests 4, 8, 12, and 16. Cracking is initially predicted in test 4 (60.0 ft/s), and grows circumferentially around the cantilever as the shock magnitude increases. By Test 12, cracking goes approximately 180° around the cantilever, but the crack has not yet propagated through to the back side of the aluminum. By Test 16, some analysis results have a crack propagating all the way through, and the cracking on the back side goes approximately from bolt 2 to bolt 6 circumferentially as shown in Figure 5-3.

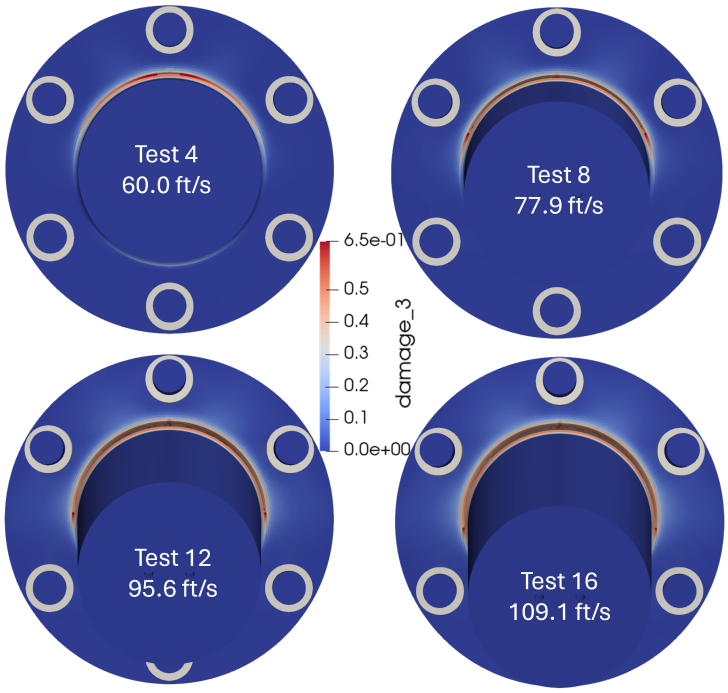

(a) Front

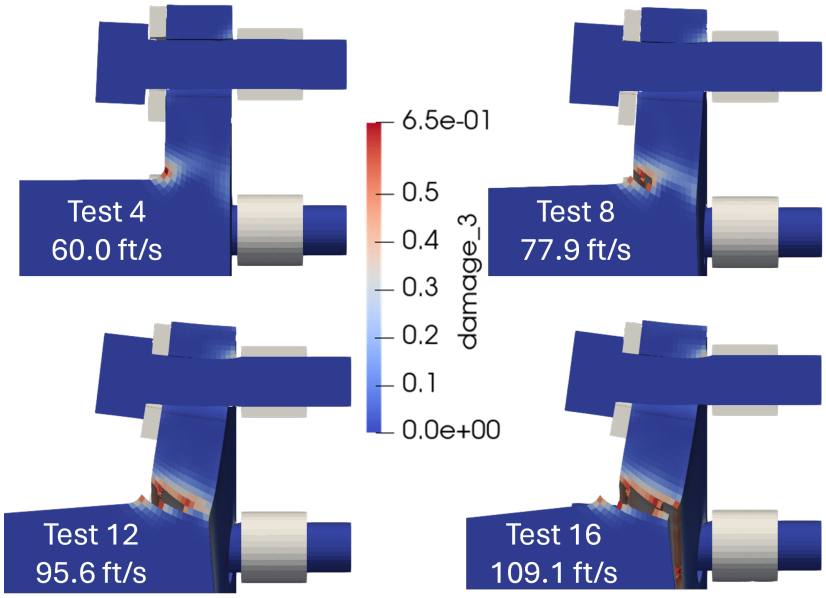

(b) Half Model - Side View

Figure 5-2. Progressive failure of aluminum cantilever for increasing shock pulse, with figures colored by *Damage*.

Failures in the SMC (cantilever cracking and fastener failure) are illustrated for the experimental and analysis results in Figures 2-6 and 5-4, respectively, where the failure mechanisms are plotted as a function of velocity change. Note that the y-axes in the two plots have slightly different categories

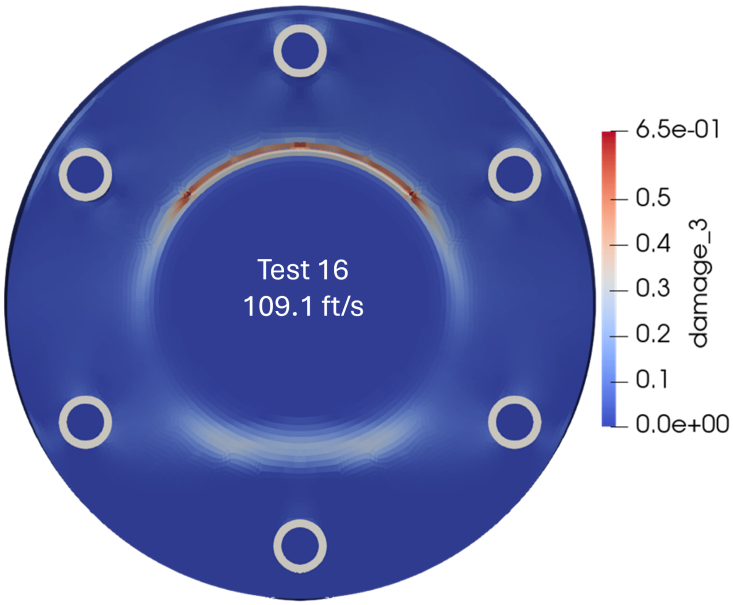

Figure 5-3. Back of cantilever for Test 16 analysis result, with figure colored by *Damage*.

for the failure mechanisms. Finding a complementary definition of "no crack" between the test and analysis is challenging, as the analysis element size limits how small of cracks can be detected in the analysis. Also note that in the analysis results, multiple samples were simulated for each test input, and thus data can exist in multiple categories (e.g. partial crack, through crack, and fastener failure for the test conducted at 105.6 ft/s).

Although the aluminum damage model is not calibrated for failure propagation, the model still provides informative predictions that are similar to test data. The analysis predictions for failure initiation seem consistent with test results. Although it is challenging to compare the "no crack" analysis category to the "small crack" experimental category, the data suggests that crack initiation might occur slightly later in the analysis (cracking begins at 60 ft/s in the analysis). This observation aligns with the overall results, as most simulation results predict that the cantilever will be significantly cracked as velocity change increases, but ultimately remain intact, while the test data has a much larger range for the "through crack" category. However, there are occasional analysis samples that predict a through crack in the cantilever in the 105-120 ft/s range. While these results under predict the damage observed in testing (the cantilever consistently experienced through cracks beyond 85 ft/s), the results are similar and would likely lead to sound engineering decisions. If failure propagation were an important quantity of interest, this region should be more thoroughly explored to capture the range of reasonable possibilities.

Partial fastener failure occurs in the analysis beginning at 98.8 ft/s, but note that this does not imply that the probability of failure of fasteners is zero below this threshold (see results in Figure 5-1). This agrees well with test data, as the range where fastener failure occurred is 105-120 ft/s. While no simulation result has all fasteners failing, this does not imply the probability of this occurrence is zero.

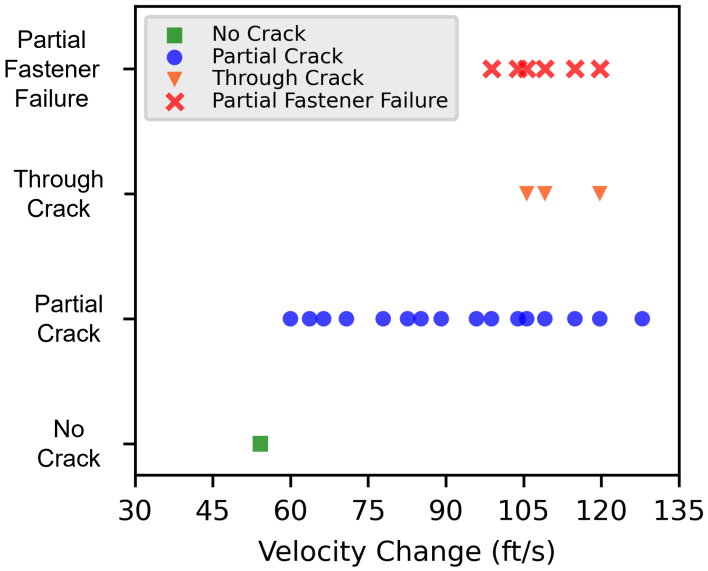

Figure 5-4. Failure mechanisms in the SMC analyses

This page intentionally left blank.

6. DISCUSSION AND CONCLUSIONS

The enhancements made to the initial SMC analysis have significantly improved the predictive capabilities of the model, demonstrating the viability and value of this approach. The new aluminum constitutive model more accurately captures the behavior of the cantilever in the drop-table tests, predicting partial and complete cracks for similar shock intensities observed during testing, although the model ultimately tends to under predict the cantilever cracking. Understanding this aluminum behavior is crucial for accurately predicting fastener failure, as these failure mechanisms appear to be interdependent.

Initial blind analysis predictions suggested a progressive failure of the fasteners that would move from the top to the bottom of the fastener array as the shock loading intensified. However, the post-blind analyses, which more accurately capture aluminum behavior, suggest that while certain fasteners (typically those at the top of the array) are still more likely to fail, the failure will not necessarily follow a progressive pattern as indicated by probabilities of failure of similar magnitudes. Although it is challenging to pinpoint the root causes of discrepancies between test and analysis due to the coupled failure mechanisms of the fasteners and cantilever, the delayed propagation of aluminum failure when all fasteners remain intact indicates potential areas for improvement in modeling failure propagation. The increased resilience of the aluminum in the analysis likely allows the fasteners to sustain more damage, resulting in slightly higher predictions for fastener probabilities of failure than what the test data suggests. However, this may not tell the whole story, as no analyses resulted in all six fasteners failing (although the results of the DD approach yields non-minuscule probability of this happening).

While the new aluminum model enhances the predictive accuracy of the simulations, capturing a comprehensive understanding of the problem would be difficult without the DD approach. Utilizing this UQ procedure, along with enhancements for bounded QoIs, enables probabilistic predictions that illustrate the deeper insights achievable through this robust and cost-effective methodology. The probabilities of failure derived from the analysis align fairly well with the test data, providing a reasonable range of velocity changes where failure is anticipated (highly probable). Furthermore, the analysis indicates that some fasteners are more prone to failure than others, and that no test within this range guarantees failure—both hypotheses are corroborated by the test data.

A significant challenge of the SMC lies in the closely linked failure mechanisms that seem to compete under more severe shock conditions. Experimental results suggest that either complete aluminum or complete fastener failure will occur, but not both simultaneously. This necessitates accurate modeling of both components to effectively capture the overall structural behavior to the degree allowed — given the significant stochastic variability in the materials and phenomena and the sparse experimental sampling of this. For the current analysis, improving the aluminum failure model could involve a more focused effort on capturing failure propagation or exploring

the uncertainties associated with the acceptable range of values for the failure criterion (see Figure 3-5).

In summary, this approach, which did not involve any calibration to the specific application problem, has demonstrated reasonable predictive capabilities that support sound engineering decision-making. The aluminum model, which more accurately captures failure and propagation, has enhanced the overall analysis predictions. Additionally, the DD approach provides a layer of knowledge and understanding that bolsters applicability of the results. The methodology is cost-effective, easy to understand, robust, and extensible, making it suitable for a wide range of applications.

REFERENCES

[1] Sharlotte L.B. Kramer, Thomas A. Ivanoff, and Edmundo Corona. Sandia mechanics challenge 2023 supplemental information packet: Structure with a threaded fastener joint. Technical Report SAND2023-10873, Sandia National Laboratories, October 2023. SAND Report.

[2] Sharlotte L.B. Kramer, Thomas A. Ivanoff, and Edmundo Corona. Sandia mechanics challenge 2023 information packet: Structure with a threaded fastener joint. Technical Report SAND2023-06848, Sandia National Laboratories, July 2023. SAND Report.

[3] E. Corona. Plasticity model calibration for steel a574 from 1/4-20 fasteners. SAND2019-12438CTF Memo to John Mersch and Jeff Smith, September 2019.

[4] J. Mersch, P. Miles, D. Najera, R. Kuether, and J. Bishop. Sandia mechanics challenge 2023 results. Technical Report SAND2024-01328CTF, Sandia National Laboratories, January 2024. Sandia Memo.

[5] Sharlotte L.B. Kramer et al. Sandia mechanics challenge 2023: Predicting mechanical behavior of a structure with a threaded fastener joint. *International Journal of Fracture*, 2025. DRAFT.

[6] V. Romero. Arguments for the generality and effectiveness of discrete-direct model calibration and uncertainty propagation vs. other calibration-uq approaches. In *Proceedings of the 24th Non-Deterministic Approaches Conference, AIAA SciTech 2022*, pages 3–8, San Diego, CA, January 2022. American Institute of Aeronautics and Astronautics (AIAA). Paper AIAA-2022-2107, also available online.

[7] J. Mersch, P. Miles, D. Fowler, C. Laursen, and B. Fuchs. Uncertainty quantification for component modeling using the discrete-direct approach. Technical Report SAND2023-08240, Sandia National Laboratories, August 2023. SAND Report.

[8] V. Romero, M. Bonney, B. Schroeder, and V.G. Weirs. Evaluation of a class of simple and effective uncertainty methods for sparse samples of random variables and functions. Technical Report SAND2017-12349, Sandia National Laboratories, November 2017.

[9] Kyle Karlson, Matthew Kury, and Reese Jones. MatCal Users Guide Release 1.3.0. Technical Report SAND2024-13395R, Sandia National Lab.(SNL-CA), Livermore, CA (United States), 2024. `http://structmechtools.cee-gitlab.lan/matcal/index.html`.

[10] AZoM. Stainless steel - grade 304, 2023-2024. Accessed: 2023-2024.

[11] Sierra Solid Mechanics Team. Sierra/solidmechanics 5.24 user manual. Technical Report SAND2025-04051O, Sandia National Laboratories, April 2025. Printed April 2, 2025.

[12] B. M. Adams, W. J. Bohnhoff, K. R. Dalbey, M. S. Ebeida, J. P. Eddy, M. S. Eldred, R. W. Hooper, P. D. Hough, K. T. Hu, J. D. Jakeman, M. Khalil, K. A. Maupin, J. A. Monschke, E. E. Prudencio, E. M. Ridgway, P. Robbe, A. A. Rushdi, D. T. Seidl, J. A. Stephens, L. P. Swiler, and J. G. Winokur. Dakota 6.21.0 documentation. Technical Report SAND2024-15492O, Sandia National Laboratories, Albuquerque, NM, November 2024.

[13] E. Friedman-Hill. The saw next generation workflow system. In *Proceedings of the NAFEMS World Congress*, number SAND2019-7344C, Quebec, Canada, 2019.

[14] LAMÉ Team. Library of advanced materials for engineering (lamÉ) votd. Materials and Failure Modeling Department, Engineering Sciences Center, Sandia National Laboratories, 2025.

[15] E. Corona, Kramer, S.L.B., B.T. Lester, A.R. Jones, B. Sanborn, and C.J. Fietek. Thermal-mechanical elastic-plastic and ductile failure model calibrations for 6061-t651 aluminum alloy from plate. Technical Report SAND2021-2983, Sandia National Laboratories, Albuquerque, NM, March 2021.

[16] E. Corona. Material model calibration and puncture calculations for 6061-t651 aluminum alloy plate. Technical Report SAND2023-11438R, Sandia National Laboratories, Albuquerque, NM, September 2023.

[17] M.L. Wilkins, R.D. Streit, and J.E. Reaugh. Cumulative-strain-damage model of ductile fracture: Simulation and prediction of engineering fracture tests. Technical Report UCRL-53058, Lawrence Livermore National Laboratory, Livermore, CA, 1980.

[18] E. Corona, M. Spletzer, B.T. Lester, and C.J. Fietek. Validation of material models for puncture of 7075-t651 aluminum plate. *International Journal of Solids and Structures*, 257, December 2022.

[19] V. Romero, C. Sanders, T. Walsh, and C. McCormick. Pragmatic uncertainty quantification and propagation in inverse estimation of structural dynamics parameters given material property uncertainties and limited sensor data. Technical Report SAND2023-12516, Sandia National Laboratories, February 2023.

[20] V. Romero and C.F. Jekel. Conservative and efficient tail probability estimation from sparse sample data. Technical Report SAND2020-7572J, Sandia National Laboratories, July 2020. Proposed for publication in ASME J. Verification, Validation and Uncertainty Quantification.

[21] V. Romero, L. Swiler, A. Urbina, and J. Mullins. A comparison of methods for representing sparsely sampled random quantities. Technical Report SAND2013-4561, Sandia National Laboratories, September 2013.

[22] V. Romero, B. Schroeder, J.F. Dempsey, N. Breivik, G. Orient, B. Antoun, J.R. Lewis, and J. Winokur. Simple effective conservative treatment of uncertainty from sparse samples of random variables and functions. *ASCE-ASME Journal of Uncertainty and Risk in Engineering Systems: Part B. Mechanical Engineering*, 4:041006–1–041006–17, December 2018.

[23] C. Jekel and V. Romero. Bootstrapping and jackknife resampling to improve sparse-data uq methods for tail probability estimates with limited samples. In *ASME 2019 Verification and Validation Symposium VVS2019*, Las Vegas, NV, May 2019.

[24] C. Jekel and V. Romero. Conservative estimation of tail probabilities from limited sample data. Technical Report SAND2020-2828, Sandia National Laboratories, March 2020.

[25] R. Jamison, V. Romero, M. Stavig, T. Buchheit, and C. Newton. Experimental data uncertainty, calibration, and validation of a viscoelastic potential energy clock model for inorganic seal glasses. In *Proceedings of the ASME Verification & Validation Symposium*, number SAND2016-4635C, Las Vegas, NV, May 2016. Presented at the ASME Verification & Validation Symposium.

[26] V. Romero, J. Winokur, G. Orient, and J.F. Dempsey. Discrete-direct model calibration and uncertainty propagation method confirmed on multi-parameter plasticity model calibrated to sparse random field data. *ASCE-ASME Journal of Risk and Uncertainty in Engineering Systems, Part B: Mechanical Engineering*, 7(2), June 2021.

[27] W. Scherzinger, V. Romero, and K. Karlson. Sandia National Laboratories ASC V&V Research Portfolio Project (2018-19): Study of Metal Plasticity Model Calibration Under Sparse Tension Test Data and Material Model-Form Uncertainty Applied to Predictions of Pressure Vessel Maximum Load.

[28] V. Romero, K. Karlson, and G. Bergel. Simultaneous discrete-direct methodology for effective treatment of sparsely sampled sources of aleatory variability and conservative estimation of tail probabilities—confirmation on a weld modeling problem. Technical Report SAND2024-01589, Sandia National Laboratories, February 2024.

[29] J. Russ, V. Romero, and R. Hopkins. Component structural dynamics model calibration and uncertainty quantification project, 2017.

[30] V. Romero. Discrete direct model calibration and propagation approach addressing sparse replicate tests and material, geometric, and measurement uncertainties. In *Proceedings of the Society of Automotive Engineers 2018 World Congress (WCX18)*, Detroit, MI, April 2018.

[31] J. Winokur and V. Romero. Optimal design of computer experiments for uncertainty quantification with sparse discrete sampling. Technical Report SAND2016-12608, Sandia National Laboratories, 2016.

[32] V. Romero. Simple, economical, effective treatment of aleatory and epistemic uncertainties involving typical information limitations in engineering projects. In *Proceedings of the 27th Non-Deterministic Approaches Conference, AIAA SciTech 2025*, number AIAA-2025-2818, Orlando, FL, January 2025.

[33] J. Mersch, E. Friedman-Hill, and K. Olson. Next generation workflow: A graphical workflow interface to increase analysis credibility and integrate expertise. In *Proceedings of the NAFEMS Americas Conference*, number SAND2024-06449C, Louisville, KY, July 2024.

[34] J. Foulk III, J. Ostien, B. Talamini, M. Tupek, N. Crane, A. Mota, and M. Veilleux. Extending a 10-node composite tetrahedral finite element for solid mechanics. In *International Journal for Numerical Methods in Engineering*, volume 122, pages 3845–3875, April 2021.

[35] G.J. Hahn and W.Q. Meeker. *Statistical Intervals—A Guide for Practitioners*. Wiley & Sons, 1991.

[36] D.C. Montgomery and G.C. Runger. *Applied Statistics and Probability for Engineers*. Wiley & Sons, 1994.

[37] W. G. Howe. Two-sided tolerance limits for normal populations - some improvements. *Journal of the American Statistical Association*, 64:610–620, 1969.

[38] Nist tolerance interval calculation web tool. `https://statpages.info/tolintvl.html`. Accessed: 2023-04-17.

APPENDIX A. Blind Prediction Calibration Results

Calibrations performed for the blind predictions are documented in Figures A-1 to A-4. Note that the end of both the red test curve and dashed blue analysis curve indicate where complete failure occurs.

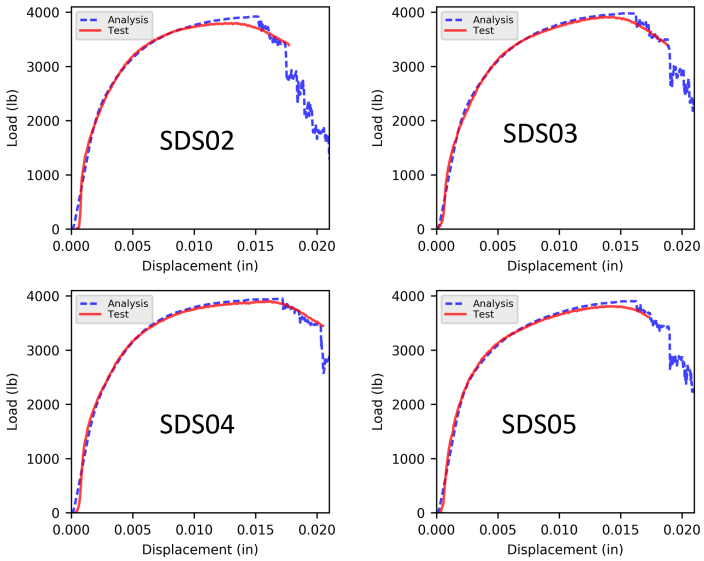

Figure A-1. Calibration results for slow double shear test data.

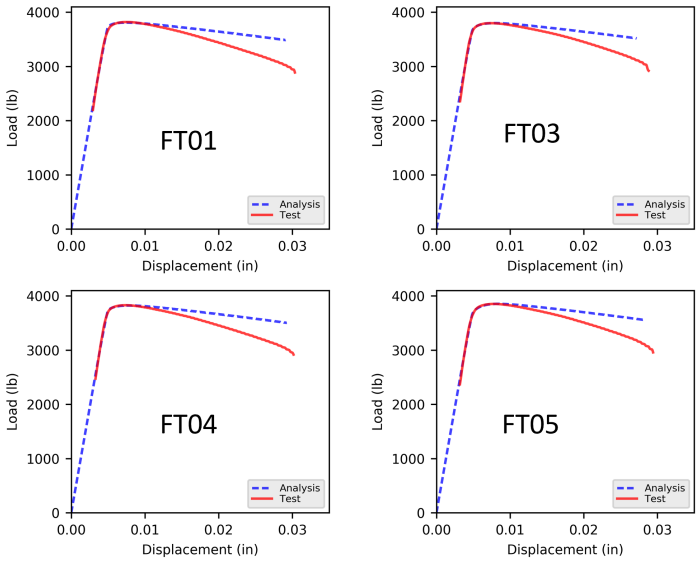

Figure A-3. Calibration results for fast tension test data

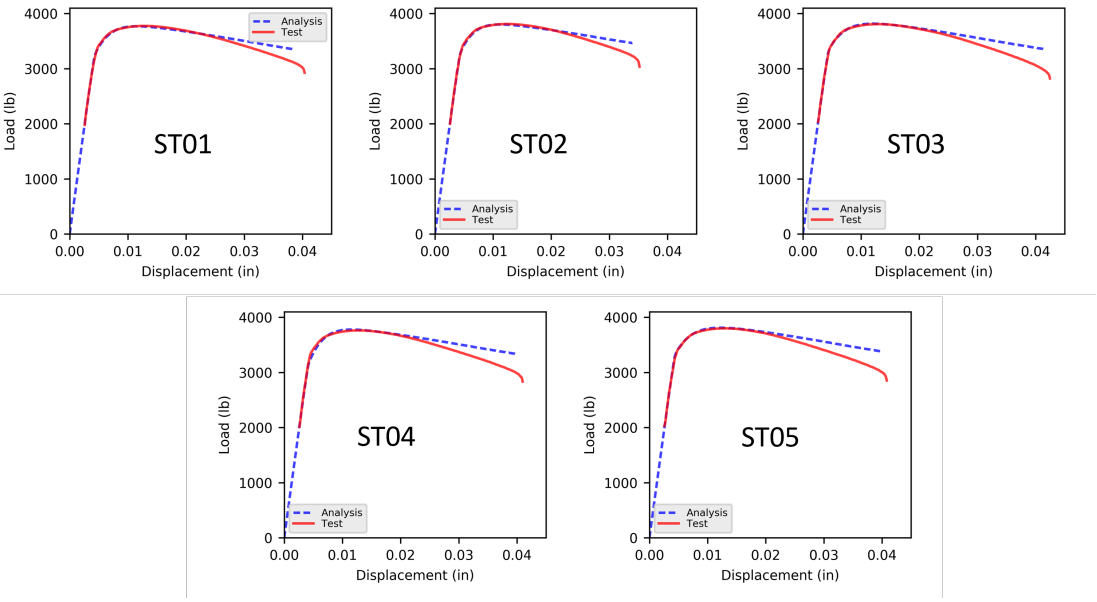

Figure A-2. Calibration results for slow tension test data.

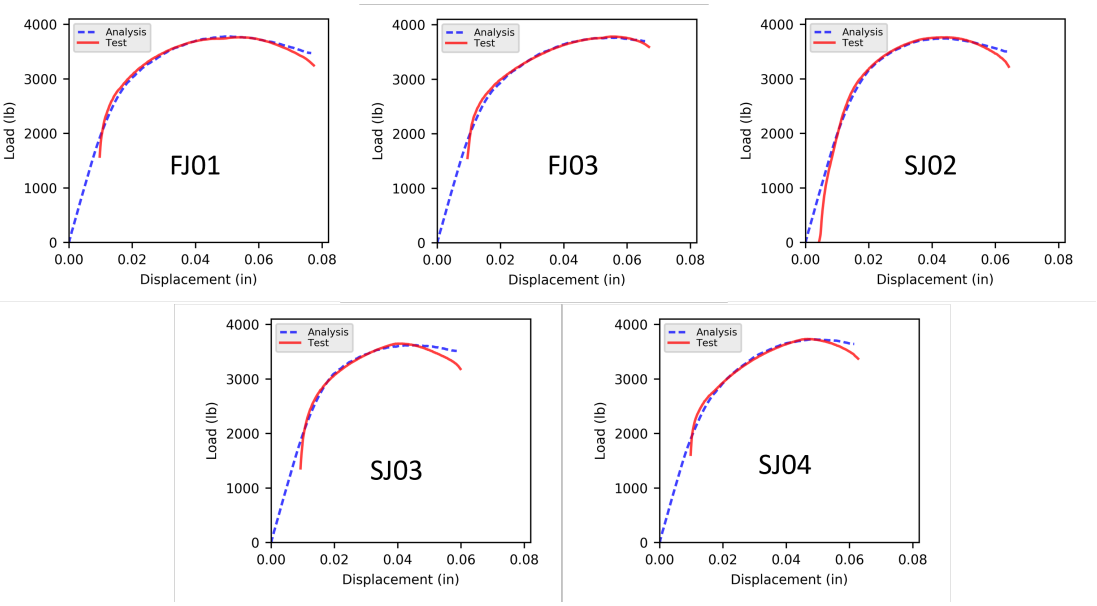

Figure A-4. Calibration results for fast/slow joint tension test data

A.1. Reasonable Bounds on Bolt Failure Probabilities from Sparse Realizations of Failures and/or Non-Failures within the Variability of Predicted Responses

Here we summarize the 1-D sparse-sample UQ methods used to obtain reasonable bounds on bolt failure probabilities from sparse realizations of failures and/or non-failures within the variability of predicted responses.

Consider the $N = 5$ fof values for each bolt in Tables 4-3 and 4-6 in Section 4.3. From a given bolt's N fof samples, we seek to conservatively estimate the proportion of fof samples that would meet the failure criterion $fof = 1$ in an asymptotically large number of material samples, tests, calibrations, and parameter set propagations in drop test simulations. In both Tables 4-3 and 4-6, Bolt 1 has two fof realizations that are 1, reaching the fof upper-bound limit in 40% of the 5 simulations in each table. To estimate the asymptotic proportion of $fof \approx 1$ failure cases in an asymptotically large number of cases, the usual 1-D sparse-sample UQ approaches studied in [20] [21] [8] [22] [23] [24] are not well suited because the distribution of Bolt 1 fof values is expected to have a substantial spike or bump at its upper end $fof \approx 1$.

For such cases, a different approach to failure probability estimation is needed. First, the fof realizations are separated into binary categories of 'failure' and 'no failure'. Even if the binomial population has a known proportion of, say, $P = 40\%$ of elements in a selected category (say failure), a relatively small number N of elements drawn from the population can have anywhere from 0 to N elements in the category.

Figure A-5 shows the analytical probability mass function (PMF) governing the various outcomes when an asymptotically large number of random trials are performed, where each trial involves $N = 5$ random draws from a binomial population containing $P = 40\%$ of instances in the failure category and the rest (60%) in the non-failure category. The PMF plot and the numbers in the caption indicate the proportion of trials that will have outcomes of 0, 1, etc., failures (listed on the plot abscissa) given $N = 5$ draws per trial.

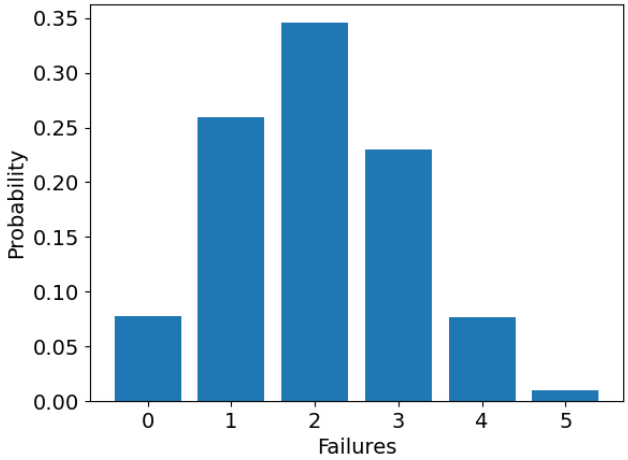

Figure A-5. Binomial distribution for $N = 5$ draws from a binomial population with $P = 0.4$. Outcome probabilities (histogram bar heights) are [0.07776, 0.2592 , 0.3456 , 0.2304 , 0.0768 , 0.01024].

The PMF in Figure A-5 shows that if the true proportion of failures in the population is $P = 0.4$, then the nominal expected outcome of 2 failures in 5 draws (0.4 proportion of failures) will occur most often, in 34.6% of the random trials. However, the probabilities of most of the other possible outcomes are also substantial.

We can iterate the parameter P governing binomial populations in order to investigate the lowest and highest reasonable values of P that would be consistent with the empirical outcome of obtaining

2 failures in 5 simulation realizations for Bolt 1. On the high end, $P_{\text{high}} = 0.74$ yields a binomial distribution/histogram with a 0.1 probability of obtaining 2 failures in 5 draws and a very high 0.98 probability of obtaining 2, 3, 4, or 5 failures. Thus, $P_{\text{high}} = 0.74$ is highly consistent with obtaining as few as 2 failures, very inconsistent (0.02 probability) with obtaining fewer than 2 failures, and non-negligibly consistent (0.1 probability) with the empirical realization of exactly 2 failures. So, it is considered a reasonable possibility that the true value of P for an asymptotically large number of material samples and tension tests, calibrations, and parameter set propagations to the drop-shock structural model could be as high as $P = 0.74$. On the other hand, $P > 0.74$ would yield less than a 1 in 10 chance of realizing the outcomes for Bolt 1 in Tables 4-3 and 4-6 in Section 5, so it is deemed outside of a range of reasonable plausibility for the true value of P.

Thus, $P_{\text{high}} = 0.74$ is deemed a conservatively high reasonable bound for a binomial large-population proportion of Bolt 1 failures in the current context. $P_{\text{high}} = 0.74$ is significantly higher than the empirical nominal failure proportion of 0.4 (2 failures in 5 realizations). For comparison, $P_{\text{high}} = 0.74$ is also vastly higher than $P = 0.353$ yielded by a 90% confidence "Tolerance Interval Equivalent Normal" (TIEN90, see below)—which would typically be a conservatively wide response-variability distribution to use unless the actual distribution has a finite bound with significant saturation of empirical samples as in the present case.

On the low end of a reasonable range for P, $P_{\text{low}} = 0.12$ yields a binomial distribution with a 10% probability of obtaining 2 failures in 5 draws and a very high 99% probability of obtaining 2 or fewer failures. $P_{\text{low}} = 0.12$ is highly consistent with obtaining as many as 2 failures, very inconsistent with obtaining more than 2 failures (0.01 probability), and non-negligibly consistent (0.1 probability) with the empirical realization of 2 failures for Bolt 1 in Tables 4-3 and 4-6. On the other hand, $P < 0.12$ would yield less than a 1 in 10 chance of realizing the said outcomes, so it is deemed outside of reasonable plausibility for the true value of P. Hence, $P_{\text{low}} = 0.12$ is deemed a conservatively low reasonable bound for a binomial large-population proportion of Bolt 1 failures.

Figure A-6 presents P_{low} and P_{high} values for this case and similarly derived values for other potential empirical outcomes of the possible numbers of failures in 4 or 5 simulation realizations. The table is relevant for the $N = 4$ or 5 calibration parameter sets from the 4 or 5 replicate tests and load-deflection data curves for each of the material-specimen geometry and loading configurations documented in [2].

The zero-failure edge cases in Figure A-6 appear to be overly conservative at the upper end P_{high}. For example, consider the fof outcomes (zero failures) for Bolt 2 in Table 4-3 in Section 4.3. The average fof is 0.728 with a standard deviation of 0.134. Using these nominal statistics from $N = 5$ samples as a rough gauge, it takes about two standard deviations from the mean to effectively reach the $fof = 1$ failure limit. As a rough estimate, if an asymptotically large distribution of fof values has the same mean and standard deviation as the $N = 5$ values in Table 4-3 and otherwise approximately normally distributed, then about 5% of the fof results would lie at the $fof = 1$ limit. This is far smaller than the 37% from Figure 20 for the highest reasonable conservative estimate of failure probability for $N = 5$ using the binomial estimation approach. Therefore, we turn to the TIEN90 approach explained next. The approach is expected to yield a conservatively wide distribution compared to an actual distribution of numerous fof realizations such that the TIEN90 would yield, to a high level of reliability or confidence as established in [20] [21] [8] [22] [23] [24],

					# of failures in N=4 random draws					
					0	1	2	3	4	
highest reasonable* asymptotic probabilit				➡	0.44	0.66	0.85	0.97	1.0	
(binomial parameter) consistent with										
≥ this # of failures in said no. of trials										
	* accompanying binomial									
	probability of this # of failures =			➡	0.10	0.10	0.10	0.11	1	
	probability of obtaining ≥ this #		failures	➡	1	0.99	0.99	0.995	1	
lowest reasonable** asymptotic probabil				➡	0.0	0.03	0.15	0.34	0.56	
(binomial parameter) consistent with										
≤ this # of failures in said no. of trials										
	** accompanying binomial									
	probability of this # of failures =			➡	1	0.11	0.10	0.10	0.10	
	probability of obtaining ≤ this #		failures	➡	1	0.995	0.99	0.99	1	
					# of failures in N=5 random draws					
					0	1	2	3	4	5
highest reasonable* asymptotic probabilit				➡	0.37	0.57	0.74	0.88	0.98	1.0
(binomial parameter) consistent with										
≥ this # of failures in said no. of trials										
	* accompanying binomial									
	probability of this # of failures =			➡	0.10	0.10	0.10	0.10	0.09	1
	probability of obtaining ≥ this #		failures	➡	1	0.99	0.98	0.99	0.996	1
lowest reasonable** asymptotic probabil				➡	0.0	0.02	0.12	0.26	0.43	0.63
(binomial parameter) consistent with										
≤ this # of failures in said no. of trials										
	** accompanying binomial									
	probability of this # of failures =			➡	1	0.09	0.10	0.10	0.10	0.10
	probability of obtaining ≤ this #		failures	➡	1	0.996	0.99	0.98	0.99	1

Figure A-6. Low and high reasonable values for the proportion of failures in an asymptotically large binomial population that yields the indicated numbers of failure realizations in the indicated number N of random draws from the population.

conservative but not overly conservative estimates of the actual proportion of $fof = 1$ bolt failures in an asymptotically large population. A TIEN90 distribution is formed as follows.

We first discuss statistical Tolerance Intervals (TIs). TIs attempt to compensate for sparse sample data by appropriately biasing toward conservative estimation of applicable width measures of the population distribution from which the samples are drawn. For instance, a useful measure is the central 95% of response between the 2.5 and 97.5 percentiles of the distribution. 95/90 TIs bound the central 95% of response with the advertised 90% confidence when based on sparse samples drawn from a Normal distribution. Lesser but still reasonable and useful success rates occur with sparse samples from a diverse variety of other distributions, including highly skewed and/or multi-modal distributions as established in [20] [21] [8] [22] [23] [24].

A X% coverage/Y% confidence TI is constructed by multiplying the calculated standard deviation $\tilde{\sigma}$ of the data samples by an appropriate factor f to create a TI of total length $2f\tilde{\sigma}$. The interval is centered about the calculated mean $\tilde{\mu}$ of the samples. Figure A-7 summarizes the construction of TIs and their "Equivalent Normal" distributions discussed in the next paragraph. The TI length scaling factor f depends on the parameters X, Y, and the number N of samples, and can be obtained from look-up tables (e.g., [35], [36]) or can be calculated from formulas (e.g., [37]) or software that

encodes the formulas, e.g., [38]. The factor $f_{90/90} = 3.52$ is used here (from [38] with Guenther sparse-sample correction).

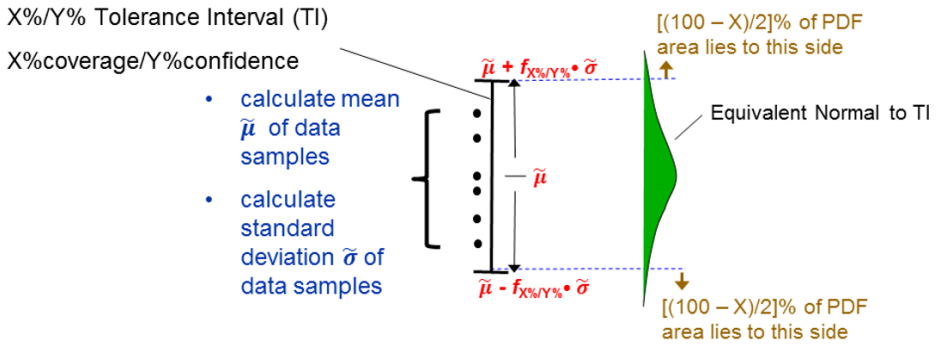

Figure A-7. Scalar data samples, tolerance interval, and equivalent normal distribution

Tail probability estimates can be based on TI methodology by forming a Tolerance Interval Equivalent-Normal distribution as illustrated in Figure A-7. For 90/90 TIs, the TI range $\tilde{\mu} \pm f_{90/90}\tilde{\sigma}$ corresponds to an estimate of central 90% coverage of the sampled population. We form a Normal distribution $N(\tilde{\mu}, \sigma_{\text{TIEN}})$ whose central 0.90 integrated probability is defined by the endpoints of the 90/90 TI. The TIEN has the same mean $\tilde{\mu}$ as the TI. By definition of a Normal distribution, the central 0.90 integrated probability of the TIEN occurs over the range $\tilde{\mu} \pm 1.645\sigma_{\text{TIEN}}$. This is set equal to the TI range to solve for the TIEN's standard deviation:

$$\tilde{\mu} \pm 1.645\sigma_{\text{TIEN}} = \tilde{\mu} \pm f_{90/90}\tilde{\sigma} \quad \Rightarrow \quad \sigma_{\text{TIEN}} = \frac{f_{90/90}\tilde{\sigma}}{1.645} \tag{A-1}$$

where $f_{90/90} = 3.52$ as stated earlier.

Effectively the same σ_{TIEN} and thus TIEN would result from a similar procedure using, say, a 95/90 TI with the same confidence specification $Y\% = 90\%$ but a different coverage specification $X\% = 95\%$ and corresponding factor $f_{95/90}$ and TIEN whose central 0.95 integrated probability lies between limits $\tilde{\mu} \pm 1.96\sigma_{\text{TIEN}}$ by definition of a Normal distribution. Thus, only the TI confidence parameter $Y\% = 90\%$ is necessary to adequately label the method. So, we use the nomenclature 'TIEN90'. Integration of a Normal distribution (such as a TIEN90) is available as a function call in most software with statistics processing capabilities such as Excel, MATLAB, and Python. We use Excel for the integration results in this document. Right-tail probability estimates are calculated as 1 minus the result of an integration of the TIEN90 distribution from $-\infty$ to the bolt failure limit $fof = 1$.

A TIEN90 based on the 5 fof values for Bolt 2 in Table 4-3 integrates to 0.170 probability of reaching/exceeding the failure threshold $fof = 1$. Analogous numbers for Bolt 3 in Table 4-3 (zero failures) are: average $fof = 0.558$, standard deviation = 0.129, and integrated TIEN90 failure probability = 0.055. The TIEN90 failure probability estimates are considerably smaller than the binomial estimate $P_{\text{high}} = 0.37$ for $N = 5$ in Figure A-6. Based on the analysis and results here, TIEN90 methodology is used for bolt failure probability estimates for Bolts 2 – 6 in Tables 4-4 and 4-7 in Section 4.3.

DISTRIBUTION

Email—Internal

Name	Org.	Sandia Email Address
Ron Manginell	1513	rpmangi@sandia.gov
Scott Roberts	1513	sarober@sandia.gov
Thomas Ivanoff	1528	tivanof@sandia.gov
Sharlotte Kramer	1528	slkrame@sandia.gov
Kevin Dowding	1556	kjdowdi@sandia.gov
John Emery	1556	jmemery@sandia.gov
Robert Kuether	1556	rjkueth@sandia.gov
Paul Miles	1556	pmiles@sandia.gov
David Najera-Flores	1556	danajer@sandia.gov
Kumar Vemaganti	1556	kmvemag@sandia.gov
Kyle Karlson	8752	knkarls@sandia.gov
Jeff Crowell	8755	jacrowe@sandia.gov
Technical Library	1911	sanddocs@sandia.gov

Sandia National Laboratories is a multimission laboratory managed and operated by National Technology & Engineering Solutions of Sandia LLC, a wholly owned subsidiary of Honeywell International Inc., for the U.S. Department of Energy's National Nuclear Security Administration under contract DE-NA0003525.